Fundamentals of Materials, Techniques, and Instrumentation for OSL and FNTD Dosimetry

M.S. Akselrod

Landauer, Inc., Crystal Growth Division, 723½ Eastgate St., Stillwater, OK 74074, USA

Abstract. The optically stimulated luminescence (OSL) technique has already become a successful commercial tool in personal radiation dosimetry, medical dosimetry, diagnostic imaging, geological and archeological dating. This review briefly describes the history and fundamental principles of OSL materials, methods and instrumentation. The advantages of OSL technology and instrumentation in comparison with thermoluminescent technique are analyzed. Progress in material and detector engineering has allowed new and promising developments regarding OSL applications in the medical field. Special attention is dedicated to Al_2O_3:C as a material of choice for many dosimetric applications. Different aspects of OSL theory, materials optical and dosimetric properties, instrumentation, and data processing algorithms are described. The next technological breakthrough was done with Fluorescent Nuclear Track Detectors (FNTD) that have some important advantages in measuring fast neutron and high energy heavy charge particles that have become the latest tool in radiation therapy. New Mg-doped aluminum oxide crystals and novel type of imaging instrumentation for FNTD technology are discussed with regard to application in mixed neutron-gamma fields, medical dosimetry and radiobiological research.

Keywords: Luminescent dosimetry, optically stimulated luminescence, nuclear track detectors, fluorescence, radiation imaging, aluminum oxide; neutron dosimetry, photon dosimetry.
PACS: 78.60.Lc; 78.55.-m; 29.40.Wk

1. INTRODUCTION

Optically stimulated luminescence (OSL), thermoluminescence (TL) and thermally stimulated exoelectron emission (TSEE) are among many known stimulated phenomena in condensed matter that can be used for passive integrating solid state dosimetry [1-5]. The detector works both as a sensor and as an information storage device (Fig. 1). No battery or electronics are needed in the dosimeter badge and it is always accumulating and safely storing the dosimetric information (it is always on!). That assures the legal dose of record without a failure. The simplified description of the process taking place during readout is illustrated by a flat band diagram presented in Fig. 2. Point defects in TL and OSL materials created during crystal growth or solid state sintering are able to trap electrons and holes generated during irradiation and in this way can store dosimetric information for a relatively long time. During the readout process the electrons or holes are released from traps (metastable states) by light or heat and recombine with their counterparts producing luminescence photons. Usually the number of emitted photons is proportional to the absorbed dose and the dose range of measurements can be as wide as 6 to 7 decades. In the case of TSEE, free electrons are emitted from the surface of the detector.

Until recently, thermoluminescence dosimetry (TLD) was the most popular dosimetric technique when relatively inexpensive passive integrating detectors based on crystalline and glass materials (like LiF:Mg,Ti, CaF:Mn, $CaSO_4$:Dy, $Li_2B_4O_7$, alumophosphate glasses and others) were used [3]. Properly packaged TL or OSL detectors combined with several different filters make the dosimetry badge a very inexpensive alternative to active electronic dosimeters with the obvious drawback of not being able to immediately display the dose and to signal an alarm in case of exceeding the preset dose rate threshold. TLD is used for personnel radiation monitoring and medical dose verification. It is a destructive technique, in that the signal is completely removed from the detector since readout

Concepts and Trends in Medical Radiation Dosimetry
AIP Conf. Proc. 1345, 274-302 (2011); doi: 10.1063/1.3576173

requires heating of a detector. Furthermore, it is slow unless laser heating is used [6], but laser heating makes already complex TLD readers even more prohibitively expensive. In addition, TL is not very suitable for high spatial resolution imaging.

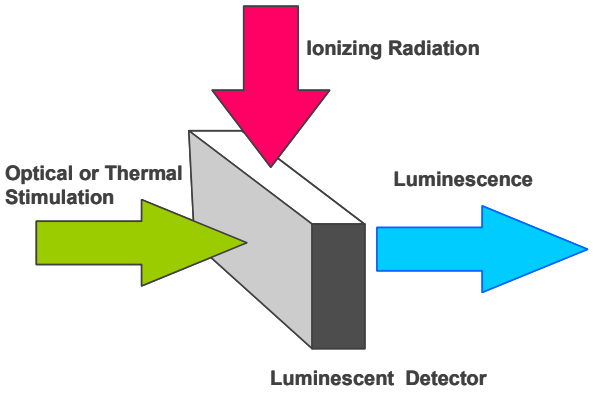

FIGURE 1. Principle of luminescent detector operation.

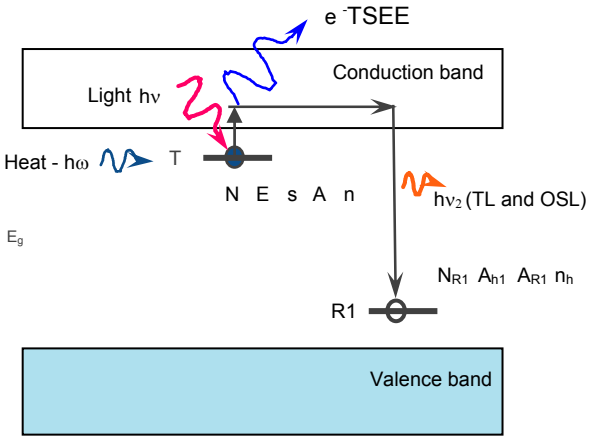

FIGURE 2. Band diagram of the electronic processes during TL, OSL and TSEE readout.

Known for decades, OSL became a successful commercial dosimetry technique after development of a very sensitive aluminum oxide (Al_2O_3:C) luminescent material [7-9] and pulsed-OSL (POSL) technique [10-12]. In contrast to TL, OSL is an all optical technique that does not require detector heating and recently developed super bright light emitting diodes (LED) allow very simple and compact OSL reader design. Due to the high luminescence sensitivity of OSL materials one does not need to empty all dosimetric traps at once. Precise delivery of stimulation light allows multiple reads with the same precision and with minimal depletion of traps. As a result, a fast and almost non-destructive readout is implemented. Because heating of the OSL dosimeter is not required, there is no detrimental effect such as "thermal quenching" of luminescence [13,14] and one can implement a simple dosimeter design by using powder-in-plastic manufacturing process with millions of OSL detectors having the same sensitivity. Ability to measure very low doses of photons and charged particles (~1μGy) with seven decades of useful dose range outweighs the downside of OSL technology - the need for light-tight packaging. Packaging as well as plastic and metal filters for photon energy discrimination are needed for any detector technology and is not a detrimental issue. Plus light sensitivity allows for fast reset of the dosimeter to erased state and quick reuse of the dosimeter without heating that very often causes degradation of sensitivity in TL materials. High resolution imaging using OSL is already widely used in digital radiography [15] and OSL imaging and image processing was successfully implemented to discriminate static and dynamic irradiation condition and to investigate the abnormal irradiations in personal monitoring [16]. Yet another unique application of OSL in medical dosimetry during radiation therapy is a remote real-time measurement using fiber-optic readout technique [17-25], and is described in detail by Dr. Claus Andersen in another paper published in this book [26].

As always, there is no one perfect dosimeter for all applications. One of the most challenging dosimetry problems is neutron dosimetry. Thermal (<0.5 eV) and intermediate (0.5 eV- 10 keV) neutrons are relatively easy to measure using TL and OSL detectors containing ^{6}Li and ^{10}B isotopes [3,27,28], but dosimetry of fast neutrons (>10keV) still remains one of the most difficult tasks. Novel fluorescent nuclear track detector (FNTD) technology is a new luminescent dosimetry technique suitable for replacing plastic nuclear track detectors (PNTD) in neutron dosimetry and LET spectroscopy of heavy charged particles [29-37]. The new technology combines a new luminescent aluminum oxide crystal, doped with carbon and magnesium (Al_2O_3:C,Mg) [38,39], with a laser scanning confocal fluorescence microscopy technique [40]. Images of tracks are formed as bright objects on dark background in fluorescent contrast and digitally processed.

1.1 Brief History of OSL

OSL was first suggested as a dosimetry tool in the 1950s and 1960s [41,42]. The main obstacles for OSL applications found at that time were: strong fading in case of relatively narrow band-gap sulfide materials like MgS, CaS and SrS doped with rare earth ions like Sm and Eu. In the 1980s the OSL technique became popular in the

archeological and geological dating community as a method of dose determination in natural materials like quartz and feldspar [43,5] Cu^{+}-doped fused quartz was suggested as a sensor for the medical fiberoptic OSL dosimetry system [23-25].

Imaging phosphors like BaBrF:Eu [15], Y_2SiO_5:Ce,Sm [44] barium phosphate doped with rare earth elements [45], KBr:In [46] and imaging techniques based on their optical stimulation with lasers were successfully developed and some of them are now used in diagnostic digital radiography. Imaging plates based on europium activated barium and strontium fluoroholides (BaBrF:Eu, BaClF:Eu and $Ba_{(1-x)}Sr_xBrF$:Eu) and readout systems are commercially produced by Fuji, Siemens, AGFA, Kodak, General Electric and other medical equipment manufacturers. The computer radiography systems that are based, in principal, on the OSL technique show excellent imaging performance but are not capable of doing precise dosimetric measurements mostly because of low thermal stability of traps resulting in relatively strong fading. Additional difficulties are caused by the high effective atomic number of BaBrF:Eu that is favorable for X-ray diagnostic imaging, but presents significant difficulties for precise measuring of doses in certain radiotherapy applications.

Recently, a new OSL dosimetry system was developed in Germany based on Thermolox™ 995 BeO material previously investigated as TL and TSEE detector [47-50]. Commercial grade ceramic chips were used as an OSL phosphor emitting UV luminescence under blue light stimulation [14,51-54].

Another type of optically stimulated charge transfer process, known as Photo-transferred Thermoluminescence (PTTL), was investigated in different materials - $CaSO_4$ [55], CaF_2:Mn [56,57], Al_2O_3:C [58], and was suggested as a dosimetric tool. However, it did not become a useful technique because of practical difficulties and low sensitivity.

The ideal OSL material should satisfy several, sometimes conflicting characteristics. It should have deep thermally stable traps for long-term storage of dosimetric information without significant fading. At the same time, these traps should be optically accessible using light sources with wavelengths well separated from the emission bands of the recombination centers. This notion implies that there is no fundamental difference between TL and OSL materials. In general all efficient dosimetric phosphors might exhibit both TL and OSL properties. The real advantage of some of the materials in comparison with the others is simply in the right combination of thermal and optical energy depths of the traps, in good separation between the emission and stimulation bands, and in a high photoionization cross-section of the traps.

Single crystals of anion-deficient Al_2O_3:C, first developed as a highly sensitive TL material [7] appeared to well satisfy all these requirements and became widely used as an OSL detector. A new pulsed-OSL (POSL) technique for radiation dosimetry using anion-deficient Al_2O_3:C has been developed [8] and is commercially implemented in Luxel™ technology and instrumentation by Landauer Inc. In addition to efficient optical discrimination between stimulation and emission light using a combination of several optical filters, a time discrimination technique is used when the laser stimulation is pulsed and the OSL is measured only during the time between laser pulses [12]. Studies of the OSL signal from Al_2O_3:C have shown it to be thermally stable and reproducible, with the detection of radiation gamma doses of 1 μGy possible. Optical bleaching may be used to "erase" the information from the material and to make it ready for the next use. Luminescent Al_2O_3:C material and an OSL technique are also used for imaging of radiation fields [10]. The latest addition to OSL family of useful dosimetric materials is BeO [14, 51-54].

2. OSL THEORY [4,5,21]

2.1 Stimulated Luminescence

The absorption of energy from an ionizing radiation source by an insulating or semiconducting material causes the excitation of free electrons and free holes and the subsequent trapping of these electronic species at defects (trapping states) within the material. After removal of the excitation the sample may then be stimulated in such a way that absorbed energy causes the liberation of charge carriers of one sign, which are then able to recombine with charge carriers of the opposite sign (see Fig. 2). The radiation absorption and the excitation of charge (primarily by the Compton effect or the photoelectron effect, depending on radiation energy and type) lead to a perturbation of the system from a state of thermodynamic equilibrium to a metastable state. The subsequent absorption of external energy by the metastable trapped charge results in the stimulated relaxation of the system back to its equilibrium condition. During the relaxation process recombination of the electronic charge occurs and, if the recombination is radiative, luminescence is emitted. In OSL, the stimulating energy source is light (UV, visible or infra-red). Normally, one monitors the intensity of the luminescence as a function of time, resulting in a characteristic

luminescence-versus-time curve. The initial intensity or the integral of the luminescence-versus-time curve is thus related to the amount of trapped charge, which in turn is proportional (in the ideal case) to the initial dose of the absorbed radiation. This is the basis for the use of OSL in radiation dosimetry.

2.2 Generalized mathematical description of optically stimulated luminescence

In OSL the luminescence intensity I is proportional to the rate at which the metastable states decay, such that:

$$I(t) = \left| \frac{d\mu(t)}{dt} \right|. \quad (1)$$

For *optical stimulation* of the trapped charge the probability p for optical stimulation at a given wavelength λ is:

$$p(E_o) = \Phi\sigma(E_o), \quad (2)$$

where Φ is the optical stimulation intensity and $\sigma(E_o)$ is the photoionization cross-section for interaction of the metastable state with an incident photon, and E_o is the threshold optical stimulation energy required to release the charge and return the system to equilibrium. In the above representations λ and Φ are all fixed values independent of time.

The various stimulation schemes are illustrated in Fig. 3 and 4. For optical stimulation, when the traps are emptied using a fixed wavelength λ and a steady illumination intensity Φ the luminescence recorded is known as *continuous wave OSL*, or CW-OSL (Figs. 3 and 4a). However, a time-dependence to p can be introduced by scanning the above terms with time - *i.e.* $\Phi(t)$ or $\lambda(t)$. Thus, for a linear increase in the intensity of optical stimulation at a fixed wavelength:

$$\Phi(t) = \Phi_o + \beta_\Phi t, \quad (3)$$

with $\beta_\Phi = d\Phi/dt$. OSL recorded is this manner is known as *linear modulation OSL*, or LM-OSL (Fig. 4b) [59].

Other schemes can be imagined in which the intensity is modulated in non-linear ways. For example, the stimulation may be pulsed, such that $\Phi(t) = \Phi_o$ for $t_0 \le t < t_0 + \Delta t$, and $\Phi(t) = 0$ for $t_0 + \Delta t \le t < t_0 + \tau$, where Δt is the pulse width and τ is the period. Such a scheme is known as *pulsed OSL*, or POSL (Fig 3c) [10,11].

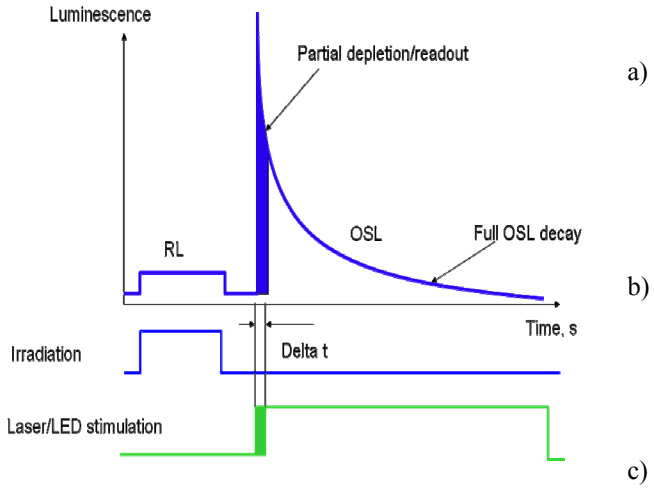

FIGURE 3. Time diagram of luminescent signal produced by OSL detector during irradiation (RL) and under continuous optical stimulation (OSL).

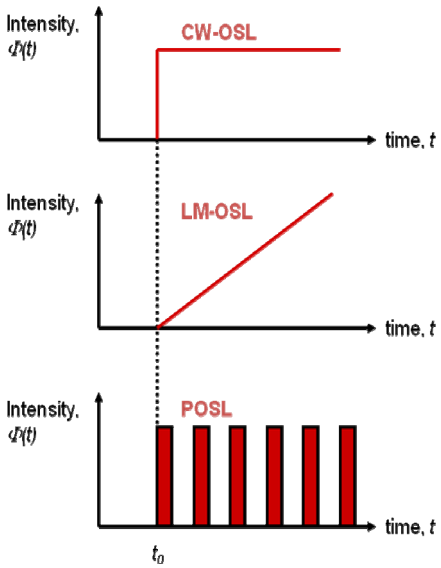

FIGURE 4. Schematic representation of the three main OSL stimulation modes, namely: CW-OSL, LM-OSL and POSL [22].

Pulsed stimulation or POSL mode (Fig. 4c) is the most recent and important innovation in OSL technology [10,12]. In CW mode separation of stimulation and emission light requires heavy optical filtration when one needs to measure single photons of luminescence in the presence of 10^{20}- 10^{22} photons of stimulation light. This heavy optical filtration reduces the amount of transmitted luminescence and reduces overall sensitivity of the readout

system. Pulsed stimulation when luminescence is measured after the pulse of stimulation is ended adds time discrimination technique to OSL and allows significantly reduce optical filtration, increases the sensitivity of the reader and improves signal-to-noise ratio (SNR) of the optical measurements. But this scheme of stimulation is applicable to only OSL phosphors with relatively long luminescence life-time like Al_2O_3:C that will be illustrated later in this paper.

2.3 The photoionization cross-section

The photoionization cross-section $\sigma(E_o)$ is perhaps the most important parameter dictating the usability of OSL material and stability of a particular trap during optical stimulation. The absorption coefficient for a defect-band optical transition at an optical stimulation energy $h\nu$ may be written as:

$$\alpha(h\nu) = n(E_o)\sigma(h\nu, E_o), \quad (4)$$

where $n(E_o)$ is the concentration of defects, each with an optical ionization threshold energy E_o. The dependence of the absorption coefficient $\alpha(h\nu)$ as a function of stimulation energy $h\nu$ should have an edge-like shape since the absorption line shape contains contributions from all the relevant continuum states in the band into which the electron is being excited [60]. Following the transition, the charge on the defect will change by one electronic charge and significant lattice relaxation may occur. This is also true during the inverse process [61].

Several expressions for the spectral dependence of $\sigma(E_o)$, namely $\sigma(h\nu, E_o)$, have been derived using a variety of assumptions relating to the potential energy in the vicinity of the defect. These and other theoretical considerations, including models with single and multiple traps, are reviewed in great details by Bøtter-Jensen et al. [5].

3. ALUMINUM OXIDE AS OSL AND FNTD DETECTOR MATERIAL

Because α-Al_2O_3:C has become the most widely used OSL detector material from now on we will describe its properties, spectroscopy, instrumentation and most important applications. Mg-doped aluminum oxide (Al_2O_3:C,Mg) is a new variety of luminescent crystals that is at the center of new Fluorescent Nuclear Track Detector technology and its optical and dosimetric properties will be considered for intercomparison with Al_2O_3:C.

3.1 Historical overview of Al_2O_3 in Radiation Dosimetry

Point defects in the form of oxygen and aluminum vacancies (F- and V-type centers respectively) and different impurities have been exploited in the various forms of α-Al_2O_3, which was introduced as a TLD dosimeter in the early 1950s. Ti-doped Al_2O_3 single crystals were first suggested as a TLD material by Rieke and Daniels [62] and further investigated by Buckman [63] and McDougall and Rudin [64]. Ceramic Al_2O_3 pellets doped with Si and Ti and processed in an oxygen-acetylene flame was reported by Mehta and Sengupta [65]. Osvay and Biro [66] made an extensive study of ceramic TLD pellets made of Al_2O_3:Mg,Y , Cr-impurity was tried by Lapraz et al. [67] and a combination of two impurities Cr and Ni in Al_2O_3 was investigated by Pokorny and Ibara [68].

However, aluminum oxide was not sensitive enough as a luminescent material until the introduction of anion-deficient and carbon-doped aluminum oxide (Al_2O_3:C). Al_2O_3:C was developed first as an ultra-sensitive TLD in the late 1980s by Akselrod et al., [7-9] and is now considered as a sensitive and practical OSL material [10-12]. It has a linearity of light output as a function of radiation dose of 7 orders of magnitude, no fading of the information due to the deep nature of the traps and extremely good environmental stability. The long luminescence lifetime (35 ms) of the F-centers in this material was successfully exploited in time-discrimination technique of POSL [12].

3.2 Defect properties in aluminum oxide

α-Al_2O_3 crystals (Fig. 5) have a rigid, slightly distorted, hexagonal-close-packed O^{2-} sublattice with Al^{3+} ions occupying two out of every three octahedral interstices (Fig. 6). Each O^{2-} ion is surrounded by four tetrahedral nearest-neighbor Al^{3+} ions. As indicated in section 2 above, the primary dose information storage process in dosimetric material is that of electronic ionization, followed by the subsequent capture of the excited electrons or holes by trapping centers. Thus, for the efficient storage of dosimetric information, it is necessary that Al_2O_3 crystals contain at least two species of defects trapping both electrons and holes. The efficient production of luminescence,

however, requires not just a high concentration of trapping sites - it also requires efficient radiative recombination pathways for electrons and holes, producing photons. In the case of aluminum oxide the innovation was the introduction of several types oxygen vacancy defects: single vacancies in case of Al_2O_3:C (Fig. 7) and double vacancy aggregate defects in the case of Al_2O_3:C,Mg (Fig. 8).

FIGURE 5. Aluminum oxide single crystals doped with both Carbon and Magnesium, Al_2O_3:C,Mg and having green coloration (left), and doped only with carbon, Al_2O_3:C (right).

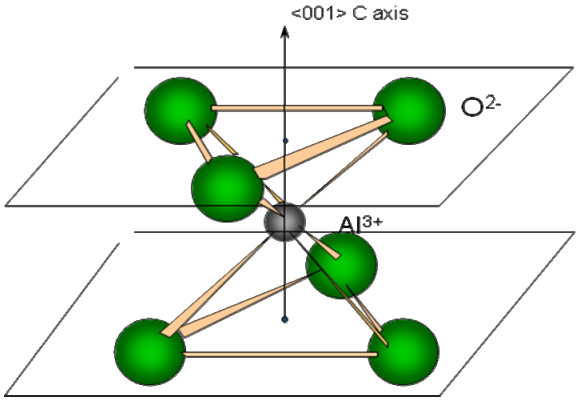

FIGURE 6. α-Al_2O_3 crystal structure has a rigid, slightly distorted, hexagonal-close-packed O^{2-} sublattice with Al^{3+} ions occupying two out of every three octahedral interstices [22].

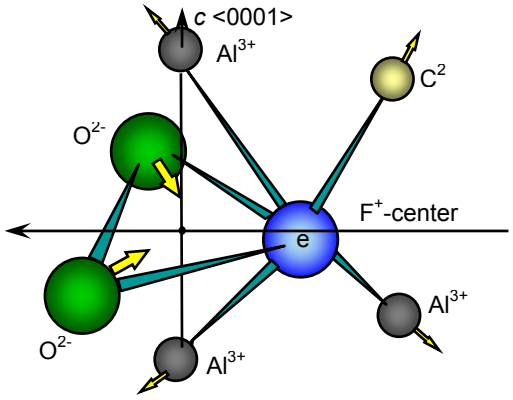

FIGURE 7. Model of F^+-center charge compensated by carbon impurity [22].

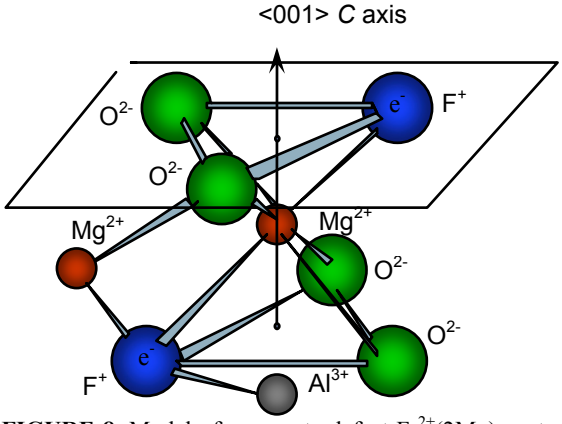

FIGURE 8. Model of aggregate defect F_2^{2+}(2Mg)-center consistent of two oxygen vacancies (two F^+ centers) and charge compensated by two Mg^{2+}-ions [38].

3.3 Defect Formation and Optical Spectroscopy of Color Centers in Al_2O_3:C

Al_2O_3 crystals can be produced by different crystal growth techniques, the most common methods are Czochralski, Edge-defined Film Growth (EFG or Stepanov), Kiropoulus, Bridgman, Heat Exchange Method (HEM). To obtain a high concentration of oxygen vacancies the crystals should be grown in a highly reducing atmosphere at a low partial pressure of oxygen. Under such conditions stable oxygen vacancies are created by the process of "subtractive coloration". Occupancy of an oxygen vacancy by two electrons gives rise to a neutral F-center, whereas occupancy by one electron forms a positively charged, with respect to the lattice, F^+-center. F-centers can be identified by strong absorption bands at 205 nm assigned to F-centers [69] and two overlapping absorption bands at 230 and 255 nm assigned to transitions in F^+-centers [70]. Oxygen vacancy defects can also be produced in Al_2O_3 crystals by neutron and high energy electron irradiation and also by thermochemical reduction (additive or subtractive coloration). F and F^+-centers are known to play a key role in the high luminescent output (TL and OSL) of Al_2O_3:C [7,9].

The reason for the success of Al_2O_3:C as a practical OSL radiation detector material is in the unique combination of several important parameters. The main fundamental advantage of Al_2O_3:C as a radiation detector is that it has a wide (9.5 eV) energy band gap, allowing one to engineer deep and thermally stable traps and color centers. Optical

absorption bands at 205, 230 and 255 nm (Fig. 9) assigned to F and F^+ centers show high concentrations of oxygen vacancies in Al_2O_3:C crystals. Mg-doped Al_2O_3 crystals have even more F^+-centers required for charge compensation of Mg^{2+} ions [38]. Study of photo-transformation of F and F^+ centers during irradiation, bleaching and annealing to different temperatures allows one to determine the type of charge carriers participating in TL, OSL and photo-transfer process [8, 71,72].

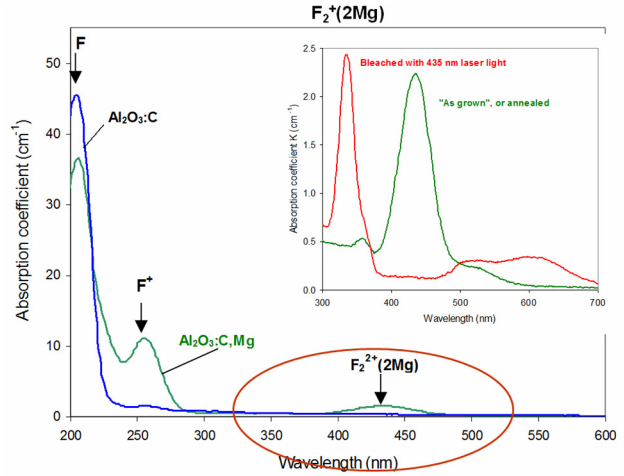

FIGURE 9. Optical absorption spectra of Al_2O_3:C and Al_2O_3:C,Mg crystals showing a significant increase in F^+-center concentration in Mg-doped crystals and appearance of new absorption bands assigned to aggregate F_2-type defects. The insert illustrates photochromic transformation F_2^{2+}(2Mg) center [38].

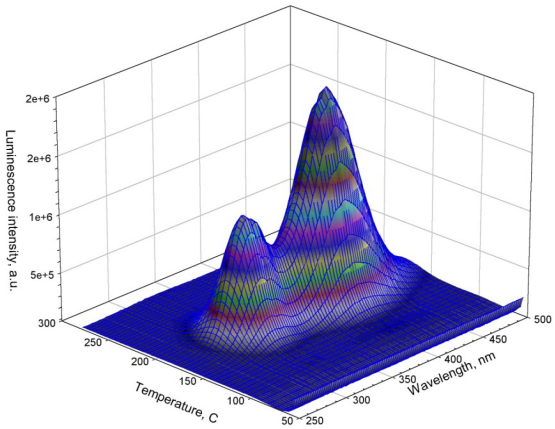

FIGURE 10. 2D Thermoluminescent spectrum of Al_2O_3:C,Mg crystal dominated by F-center (420 nm) and F^+-center (330 nm) emissions.

F-centers produce luminescence at 420 nm with a long (35 ms) lifetime, whereas F^+-center emission is centered at 330 nm (Fig.10) and has an extremely short lifetime (<7ns). It was found that an increase in the concentration of F^+-centers in Al_2O_3:C causes increase in OSL and TL sensitivity. It was suggested that oxygen vacancies in the form of F^+-centers are created in Al_2O_3 doped with carbon during crystal growth in a highly reducing atmosphere as a result of charge compensation of divalent carbon ion substituting trivalent Al^{3+}-ion [7]. One of the possible configurations of this defect is depicted in Fig. 7. It is important to mention the effect of thermal quenching of F and F+ center luminescence that reduces the yield of TL in Al_2O_3 at a high heating rate. Evans and Staplebroeck [69] showed this effect for F^+-centers and Akselrod *et al.* [13] for F-centers. The OSL process is not affected by thermal quenching, however, resulting in a significant gain in light output in comparison with TL [73,74]. Optical absorption and emission-excitation spectroscopy was used to identify the nature of trapping sites and recombination centers in Al_2O_3:C [8,72,75,76].

Mg-doped aluminum oxide with aggregate defects has many more optical bands. Photochromic and radiochromic transformations in this crystal are more complex but also bring more interesting physics and the possibility for new applications [29-39]. Figure 11 illustrates the proposed assignment of defects to emission-excitation bands in Al_2O_3:C,Mg crystals and radiochromic transformations of these defects after the irradiation. In addition to single vacancy defects (F and F^+-centers) dominating in Al_2O_3:C double vacancy defects (denoted as F_2 type centers) associated and not associated with Mg-impurity ions were identified and assigned to different emission-excitation and absorption bands. The most important advantage of this new crystal for practical application is that these color centers undergo efficient radiochromic transformations. As a charge storage they are thermally deep and stable up to 600 ºC. The lifetime of their luminescence is short (9 ns for F_2^{2+}(2Mg) center emitting at 520 nm and 75 ns for F_2^+(2Mg) center emitting at 750 nm) which allows for fast laser scanning in imaging applications [38]. That is almost a million times faster than the 35 ms lifetime of F-center luminescence in Al_2O_3:C which in turn has an important practical advantage for time discrimination in the POSL technique [12]. Double vacancy defects are optically stable and can be interrogated multiple times without photoionization which provides non-destructive readout using intra-center fluorescence (see later section 5.1 and Fig. 34), or if it is radiation-induced it is called radio-photo-luminescence (RPL). This is in contrast with the OSL process including one in Al_2O_3:C where photoionization of traps (optical stimulation) followed by recombination of charge on luminescent centers and

results in destructive readout. Both physical processes – intra-center fluorescence, and recombination luminescence during OSL readout, have their own practical advantages and disadvantages.

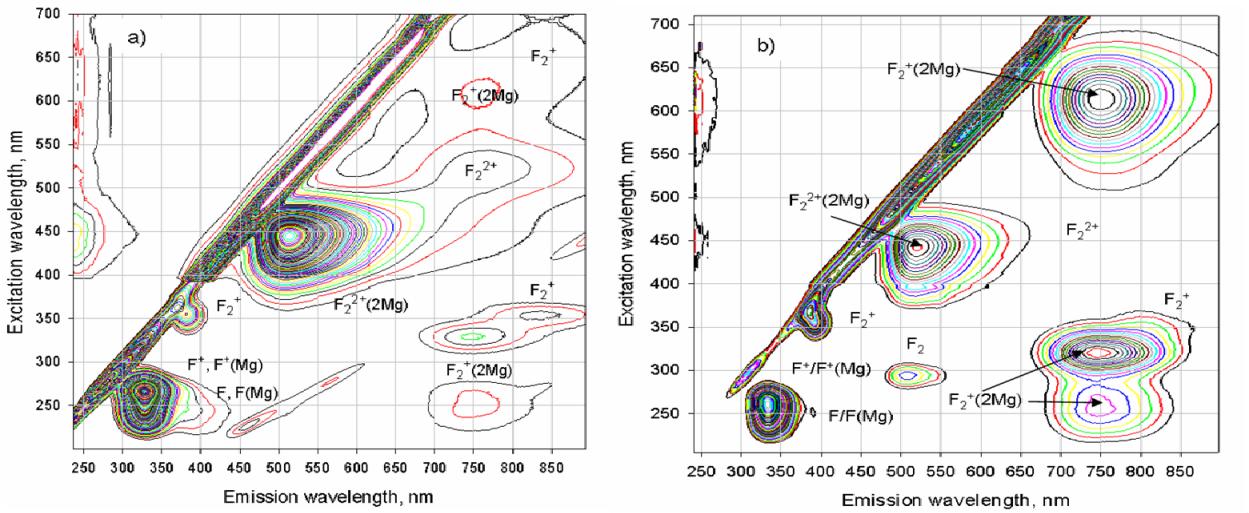

FIGURE 11. Emission-excitation spectra of Al_2O_3:CMg crystal before and after irradiation with 143 Gy of $^{90}Sr/^{90}Y$ beta [90].

3.4 Dosimetric Properties of Al_2O_3:C for OSL Applications

The dosimetric TL peak in Al_2O_3:C measured at a heating rate of 5K/s is located at 450 K (Fig. 14) [7,11]. Thermal activation energy obtained from TL peak analysis is estimated around 1.5 eV. The electron trap associated with this TL peak is very stable at temperatures close to room temperature with a measured fading rate of less than 5% per year. At the same time the optical depth of this trap, determined from photostimulated exoelectron emission measurements is not very large and is equal to 2.2 eV [9]. This determines the range of wavelengths suitable for optical stimulation [71]. Although the most efficient wavelength for OSL stimulation of Al_2O_3:C is in the blue region [75], a need to discriminate the stimulation light from the broad F-center emission centered at 420 nm (Fig. 10) determines the use of green stimulation with sources of light like the 532 nm second harmonic of a Nd:YAG laser, the 514 nm line of an Ar-ion laser or InGaN LEDs with a peak wavelength at 527 nm. In practical OSL readers single photons of luminescence are detected in the presence of up to 10^{20}-10^{22} photons of stimulation light and good optical separation and filtration is required.

A high sensitivity to radiation (determined as a number of emitted luminescence photons per unit of absorbed dose), allows OSL dosimetry system based on Al_2O_3:C to achieve the low limit of detection of less than 1 μGy [7,12] and 7 decades of useful dose range of linearity of dose dependence (Figs. 12 and 13), that can be achieved with a simple instrumentation method by automatically changing intensity of stimulation light [12]. A low background signal under optical stimulation, and an acceptable photoionization cross-section of traps at the chosen wavelength are among the important dosimetric parameters of Al_2O_3:C. Al_2O_3:C is an erasable OSL material and can be reused multiple times after optical bleaching or thermal annealing. Bleaching kinetics are not first-order, and the OSL decay not described by a single-exponential (Fig. 16). This is probably a result of a relatively wide distribution of optical activation energies [75]. Filling of deep traps during high dose irradiation [7,8,72,76] can create some difficulties when performing complete optical bleaching and may require high temperature annealing to completely zero the detector and reduce the background OSL signal caused by so-called "dark transfer" or leakage from the deep traps. These dark transfer processes are well known in TL materials [3]. It is not always possible to empty deep traps in aluminum oxide embedded in plastic (see below the instrumentation section). Because powder-in-plastic Al_2O_3:C OSL detectors are so inexpensive one does not need to reuse a dosimeter after high dose exposure.

It has been shown that the same traps in Al_2O_3:C are responsible for both OSL and TL production. The single TL peak at about 450 K is produced after gamma-irradiation and UV excitation (although the TL peak shape after UV irradiation is not the same as that after irradiation with gamma). Two types of shallow traps, responsible for TL peaks at 260 and 310 K, have also been reported [9,11] and their concentration was significantly reduced in Al_2O_3:C material of OSL quality (Figs. 14 and 22).

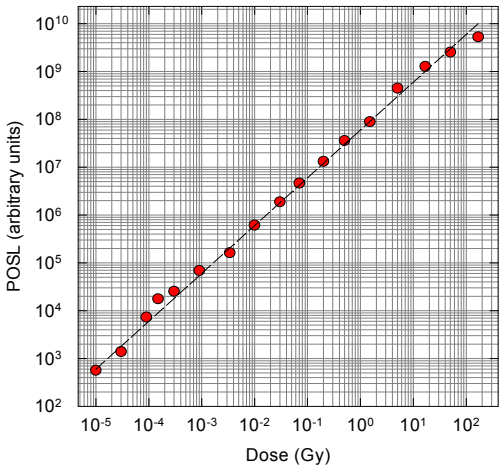

FIGURE 12. Dose dependence of POSL signal from Al_2O_3:C demonstrating 7 decades of useful dose range from 1 μGy to 100 Gy [10].

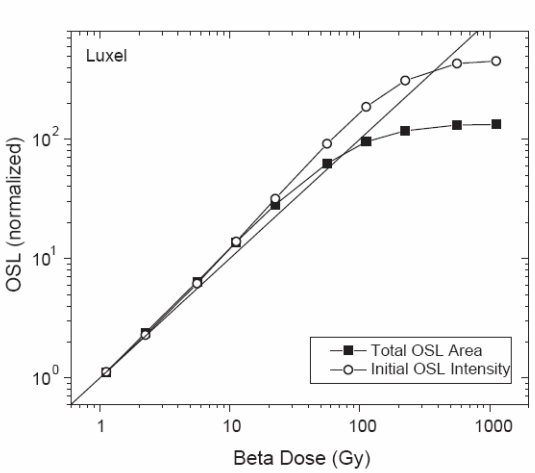

FIGURE 13. OSL dose response of Al_2O_3:C Luxel detectors to beta radiation. The initial OSL intensity corresponds to the first 3 s of integration and the total OSL corresponds to integration for 300 s [72].

The existence of both shallow and deep traps in Al_2O_3:C affects the performance of the material as an OSL detector. For example, shallow traps in different types of Al_2O_3:C developed for TL, OSL and "delayed" OSL (DOSL) applications were investigated using the TL technique after irradiation at liquid nitrogen temperatures (Fig. 14). Retrapping of delocalized charges in the shallow traps reduces the probability of radiative recombination and slows the OSL decay. Shallow traps also introduce a temperature dependence to the OSL measurements such that different OSL decay curve shapes are obtained if stimulated at different temperatures [11].

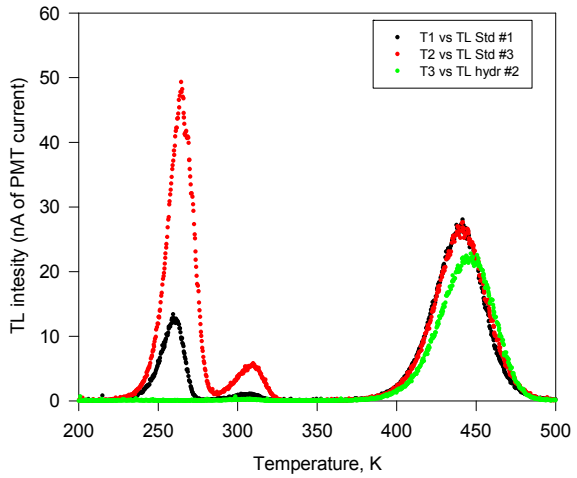

FIGURE 14. TL from three different types of Al_2O_3:C crystals with low, medium, and high concentration of shallow traps. For OSL application a minimum concentration of shallow traps is desired [11].

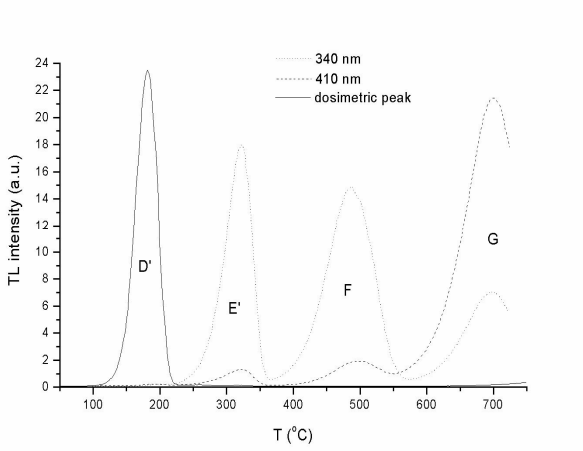

FIGURE 15. Deep traps in Al_2O_3:C indicating themselves as TL peaks obtained after 205 nm UV illumination at elevated temperature and measured through 340 and 410 nm interference filters [77].

The existence of several efficient deep traps with delocalization temperatures at approximately 680, 770, 920 and 1170 K were identified using methods of photo-transferred thermoluminescence [8,76], high temperature TL [77] and photoconductivity [75]. One of the ways to determine the thermal energy ("depth") of the deep traps is to measure TL after high temperature irradiation, as depicted in Fig. 15 [77]. Deep traps affect the OSL process in different ways. Firstly, they compete for charge carriers during irradiation. This in turn causes changes in the OSL sensitivity as the deep traps are filled during the irradiation period. Whether the sensitivity increases or decreases as

the deep traps fill depends upon whether the deep traps are holes traps, or electron traps, both of which are known to exist in this material. Yukihara et al. [76] demonstrated that in some samples the hole traps dominate and thus the sensitivity is smaller after deep trap filling compared with when all traps are empty. This results in sublinearity of dose response at high doses. Conversely, in samples in which the deep electron traps dominate over the deep hole traps, the sensitivity increases with deep trap filling and the dose dependence shows supralinear behavior (see Fig. 13). Secondly (as already noted) the deep traps (specifically the electron traps) are responsible for charge photo-transfer and a residual OSL signal that is difficult to eliminate using optical bleaching when using stimulation wavelengths normally used in OSL measurement.

Another important feature of OSL using Al_2O_3:C is its ability to be reliably re-read (Figs. 16 and 17). Thus, the dose may be independently measured multiple times from the same detector. This arises from the high sensitivity of the method such that each OSL measurement only empties a fraction of the trapped charge available. The accumulated amount of charge on the dosimetry traps is so large that it is possible to precisely read the dose using only 0.2% of the total OSL signal. Depletion kinetics remain constant for the low dose range (up to 1 Gy) and allow one to perform precise dose re-estimation, after correction for partial trap depletion [12]. For practical dosimetry applications this feature of OSL technology allows one to re-evaluate the doses almost non-destructively.

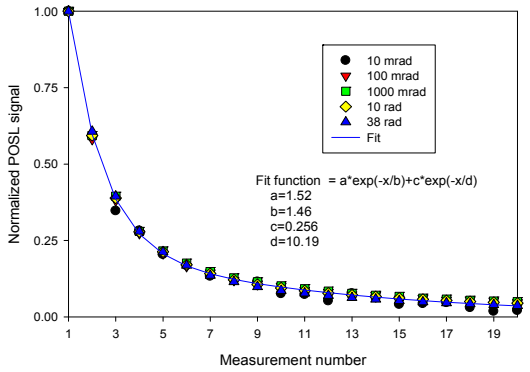

FIGURE 16. The OSL decay curve from Al_2O_3:C has a reproducible shape for doses below 1 Gy and multiple dose re-estimation is possible with the same precision as the first readout [12].

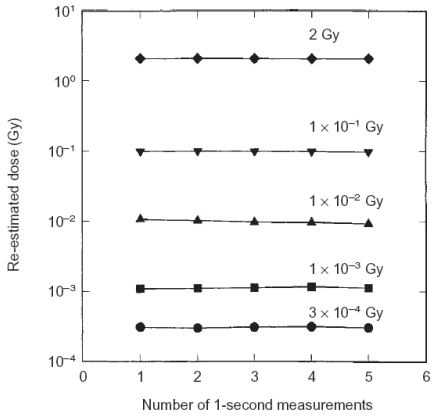

FIGURE 17. Reproducibility of multiple OSL re-reads at different doses using 1 s stimulation and depletion correction function of Fig 16 [12].

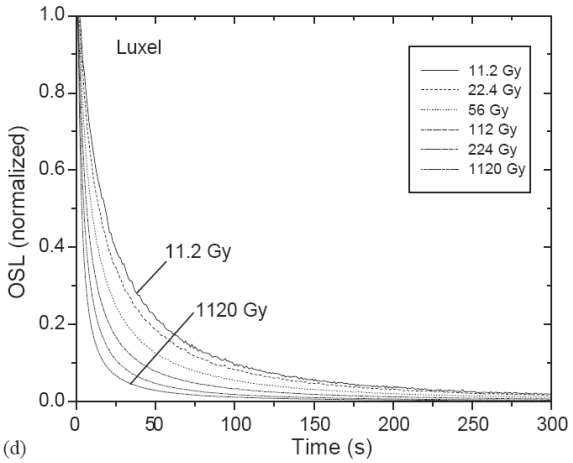

FIGURE 18. At high doses the OSL decay curve from Al_2O_3:C changes shape which allowed the development of a technique to measure the LET of the heavy charge particles [78].

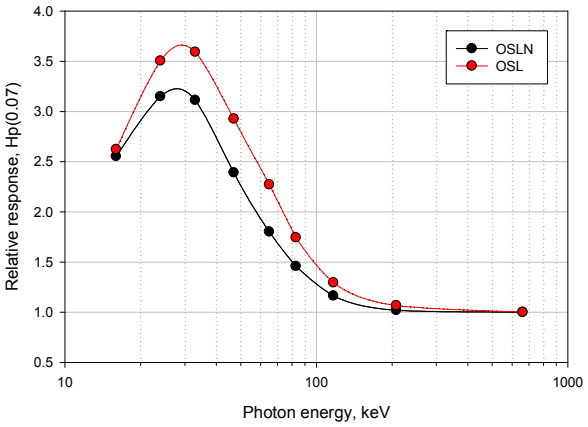

FIGURE 19. Energy response of OSL and OSLN Al_2O_3:C InLight™ dosimeters. OSLN materials is a neutron sensitive composite material consisting of Al_2O_3:C and $^6Li_2CO_3$ that works in albedo configuration. All measurements are done with detectors covered with 300 mg/cm^2 of plastic [79].

Aluminum oxide is not a tissue-equivalent material with effective atomic number (Z_{eff}) of 10.2 and density of 3.96 g/cm^3 that is higher than for tissue and water. Higher mass-absorption coefficients of the detector material causes the OSL detector to over-respond at low energy photons vs. 662 keV gamma photons of ^{137}Cs (Fig. 19). This energy dependence is actually a beneficial factor for selecting filters in dosimeter design, for discriminating low and high energy photons, and for the algorithm of calculating the dose equivalent.

Until recently Al_2O_3:C OSL detectors were used only for photons and beta radiation. Measurements of neutrons using OSL became possible with the development of neutron sensitive material (OSLN) in which grains of Al_2O_3:C are coated with Li_2CO_3 material enriched with ^{6}Li isotope [27,28]. The new phosphor is a 50:50% composite of Al_2O_3:C and $^6Li_2CO_3$ obtained by fusion of two compounds followed by crashing and grinding. The final OSLN sensor is obtained by printing of the OSLN powder mixed with polymer binder on a plastic substrate the same way the regular OSL detectors are produced in mass quantities. OSLN detectors are mostly sensitive to low energy neutrons and their neutron energy dependence of sensitivity follows the (n,α) nuclear reaction cross-section of neutrons on ^{6}Li. Figure 20 shows the results obtained after monoenergetic neutron irradiations at NPL (UK) and JRC-IRMM (Belgium).

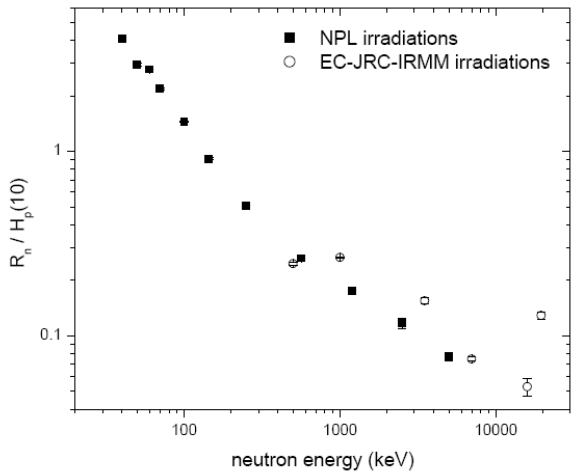

FIGURE 20. Normalized OSL signal as a function of neutron energy for OLSN material that is 50:50% composite of Al_2O_3:C and $^6Li_2CO_3$. [80].

3.5 POSL Technique

Pulsed OSL technique [10-12] provides an efficient method of radiation dosimetry with a wide dynamic range, high sensitivity and excellent signal-to-noise ratio (SNR). Important considerations are the choice of stimulation pulse width and repetition rate (frequency). By choosing these appropriately for the material under study one can optimize the measurement parameters so that very high luminescence detection efficiency can be obtained. The fundamental requirements for high detection efficiency is that the material luminescence lifetime is longer than the stimulation pulse width plus the 'dead' time needed for the PMT to relax after the pulse of light.

Figure 21 schematically shows the synchronous detection arrangement in which a stream of laser pulses is synchronized with a PMT counter gate so that during the pulse, and for a short period before and after the pulse, the data acquisition is switched off. Data acquisition occurs only for a predefined period between pulses. The PMT is kept on at all times and only the photon counter gated so as to count pulses only during the specified period. There is no need to wait until the POSL signal from a given pulse has decayed away before the next pulse arrives. Furthermore, since the pulse width (300 ns in this example) is very much less than the luminescence lifetime, an insignificant amount of light is lost by switching off the data acquisition during each pulse. At the frequency 4000 Hz the total dead time for a 1 s stimulation period is ~60 ms and the loss of luminescence is only 6%. The net result is a very high measurement efficiency combined with good SNR and relaxed requirement for optical filtration of stimulation light. In practice one seeks to maximize the luminescence emitted after the pulse compared with the luminescence emitted during the pulse by reducing the pulse width and increasing the peak laser or LED power. However, the PMT still should be protected by optical filters from being blinded by the stimulation pulse.

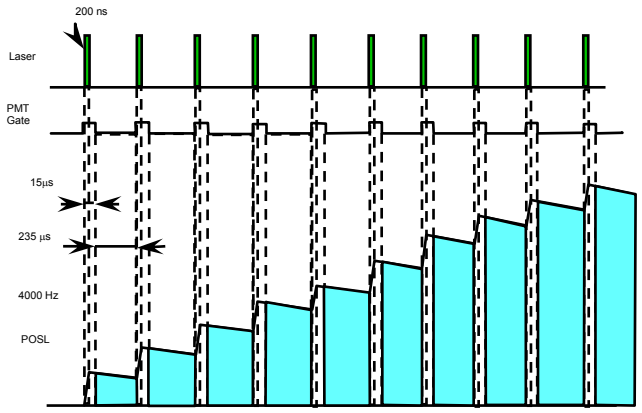

FIGURE 21. Schematic of the timing diagram to synchronize the POSL measurement with the Nd:YAG laser pulses. The shaded regions in the lower part of the diagram indicate the periods of luminescence measurements. In each of these periods (235 μs long) the luminescence decays with a 35 ms lifetime. The sum of all the counts recorded during these data acquisition periods forms the measured POSL signal [12].

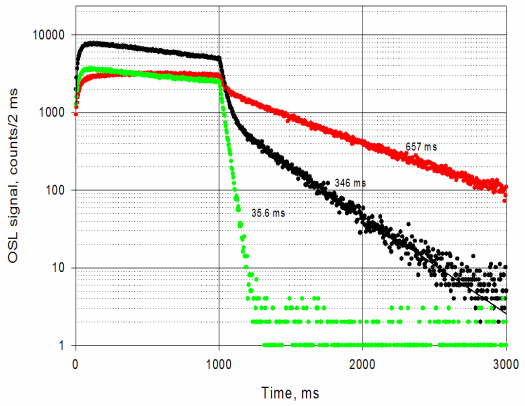

FIGURE 22. Kinetics of POSL signal during 1000 ms of pulsed laser stimulation, followed by 35 ms decay of F-center luminescence and temperature dependent phosphorescence from shallow traps, sometimes called Delayed OSL (DOSL). Three curves represent materials with different concentration of shallow traps [11].

There is an important implication of the long 35 ms luminescence lifetime and shallow traps concentration on the shape of the POSL signal as depicted in Fig. 22 for three different Al_2O_3:C crystals. First the POSL signal increases with the stimulation time. At some point equilibrium between the rate of excitation of luminescence centers and the rate of relaxation decay of such centers is achieved. Eventually the signal decreases due to trap depletion, but this decrease strongly depends on the shallow traps concentration. OSL material with a higher concentration of shallow traps show slower decay during stimulation due to retrapping of charge and exhibit a long tale of phosphorescence after the optical stimulation is turned off at t=1000 ms. Another implication of the presence of shallow traps is a slight temperature dependence of the measured luminescence due to phosphorescence that is a thermally stimulated process [11].

3.6 OSL Imaging Technique

One of the many advantages of the OSL technology is its imaging capability already utilized in computer radiography [15]. In personal monitoring abnormal exposure condition of interest is the accidental or intentional (i.e. unauthorized) exposure of the dosimeter to a radiation source when the dosimeter is not being worn by a person. An example would be provided by someone placing the radiation dosimeter close to a radiation source in order to expose the dosimeter, but not the person. Such “static" exposures of the dosimeter will produce a sharp image of the filters positioned in front of the OSL film. This is to be distinguished from an exposure in which a person wears the dosimeter on his/her clothing over an extended period. Other potential abnormal exposure conditions include the unintentional shielding of the dosimeter by external objects (coins, paper-clips, etc.) due to the dosimeter being worn incorrectly (say) in a person's pocket rather than being worn correctly on the outside of a person's clothing. Other abnormal exposure conditions include angular irradiations or contamination of the dosimeter by radioactive contaminants.

The method for the distinction between the normal, “dynamic" radiation exposure and an abnormal, or ”static", exposure of the dosimeter in a fixed position relative to a radiation source is illustrated by Fig. 23 and is described in detail in [16]. The technique relies upon the use of a radiation filter with a periodic array of holes, or other weakly absorbing regions, such that the Al_2O_3:C is exposed in a pattern which follows the pattern of the filtration. Subsequent illumination of the Al_2O_3:C reveals a pattern of luminescence emission corresponding to the pattern of the absorbed dose. During static exposure, the absorbed radiation pattern is sharp and contrast, whereas during dynamic exposure the absorbed radiation pattern is diffused. Image processing of the collected POSL emission pattern using a Discrete Fourier Transform produces a spatial frequency spectrum of the collected image from which a factor is calculated which indicates the probability of static versus dynamic exposure. Furthermore, the POSL

image obtained can also reveal accidental shielding. The image collection procedure, the image processing algorithms, and two different methods to determine the probability factor are described in details in [16].

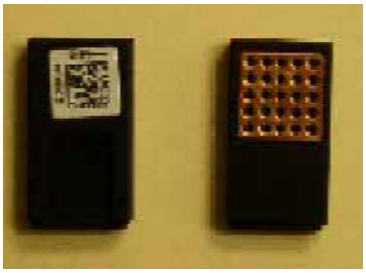

a) Photo of Landauer imaging OSL element;

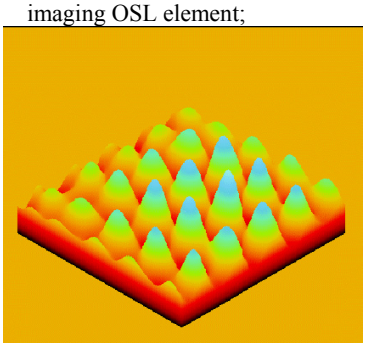

b) OSL image after static X-ray exposure;

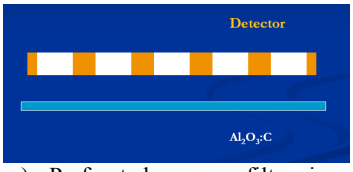

c) Perforated copper filter is spaced from OSL detector;

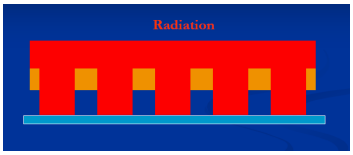

d) After static exposure the image is strongly spatially modulated;

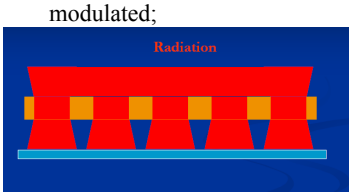

e) After dynamic exposure the image is blurred;

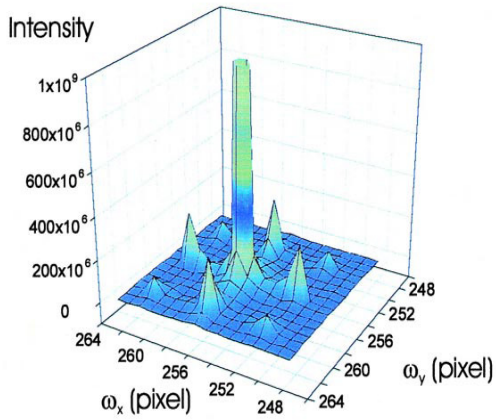

f) Power spectrum of OSL image with characteristic spatial frequencies corresponding to filter grid spacing [16].

FIGURE 23. Imaging OSL element and a diagram explaining difference between static and dynamic X-ray exposures that can be identified by the image processing in spatial frequency domain and raise a flag in case of high dose and static exposure.

3.7 OSL Dosimeters and Instrumentation

The first commercial OSL dosimeter, promoted as Luxel™, based on the POSL technique and Al_2O_3:C was developed for occupational personnel dosimetry, and introduced by Landauer in 1998. The sensitive element of OSL dosimeter is Al_2O_3:C powder mixed with an organic binder and printed on a transparent plastic substrate. In the latest modification depicted in Fig. 24a, the OSL sensor is sandwiched between two parts of a clamshell filter pack having 5 detector areas with different filtration: open window, plastic, copper-aluminum, aluminum and a central imaging element made from a perforated copper plate. The imaging element allows a service provider to distinguish between static and dynamic exposures using patented image processing algorithm [16].

InLight™ dosimeters use the same Al_2O_3:C printed OSL material as Luxel™, but punched as 7 mm disks and mounted in slides and cases with four different filters (Fig 24b and 24d). An imaging component with a perforated copper filter and/or CR-39 neutron detector can be added to the dosimeter during assembly. The Nano-Dot – a small form-factor OSL detector having a light-tight case with a size of only 10×10×2 mm is designed for medical dosimetry, radiation equipment quality assurance (QA) and patient monitoring (Fig. 24c). The Nano-Dot can be read on the same micro-Star reader as an InLight™ dosimeter using a special adapter.

a) Luxel™;

b) InLight™ dosimeter;

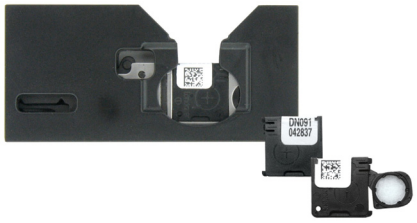

c) Nano-Dots and adapter for the microStar InLight OSL reader;

d) InLight™ dosimeter components

FIGURE 24. Different OSL dosimeters from Landauer, Inc.

One of the main concerns in medical diagnostics using X-rays is a potential patient overdose. Once again OSL technology can be used to prevent it from happening. A strip OSL dosimeter is used for quality control of Computed Tomography (CT) scanner (Fig. 25). The OSL strip dosimeter fits in FDA phantom for exposure inside the CT scanner with predetermined parameters. The OSL strip measures dose profile with a high spatial resolution of 0.1 mm and provides information on collimation, profile of individual slice, and slices overlap.

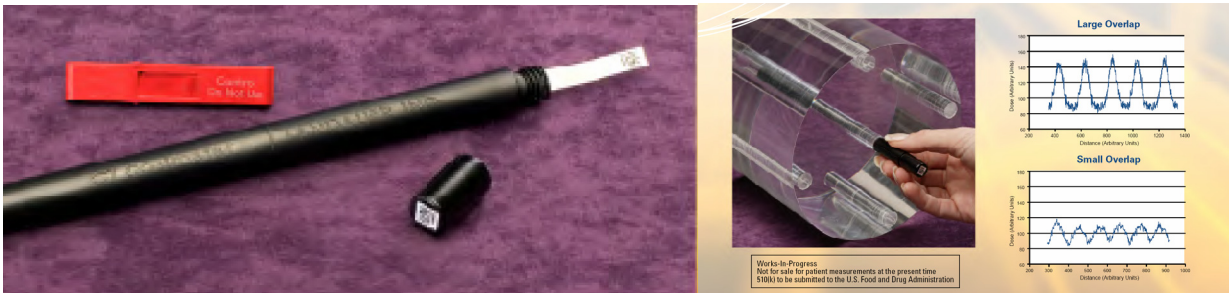

FIGURE 25. Computed Tomography quality control using Landauer OSL strips.

3.8 OSL Readout Instrumentation

At the introduction of the POSL technology in the 90s the readout instruments were relatively complex and expensive, mostly because of the high cost of pulsed Q-switched Nd:YAG lasers, but recently superbright green LEDs with good modulation properties were introduced and allowed the for the development of a new generation of

instrumentation. Figures 26 and 27 show two examples of OSL instrumentation. InLight™ microStar is a compact instrument for manual inserting and reading of InLight™ dosimeters and Nano-Dots using an additional adapter. microStar is used by small labs and hospitals, whereas automatic InLight™ Auto200 and Auto500 (not shown) readers were designed for relatively large scale operations at dosimetry laboratories.

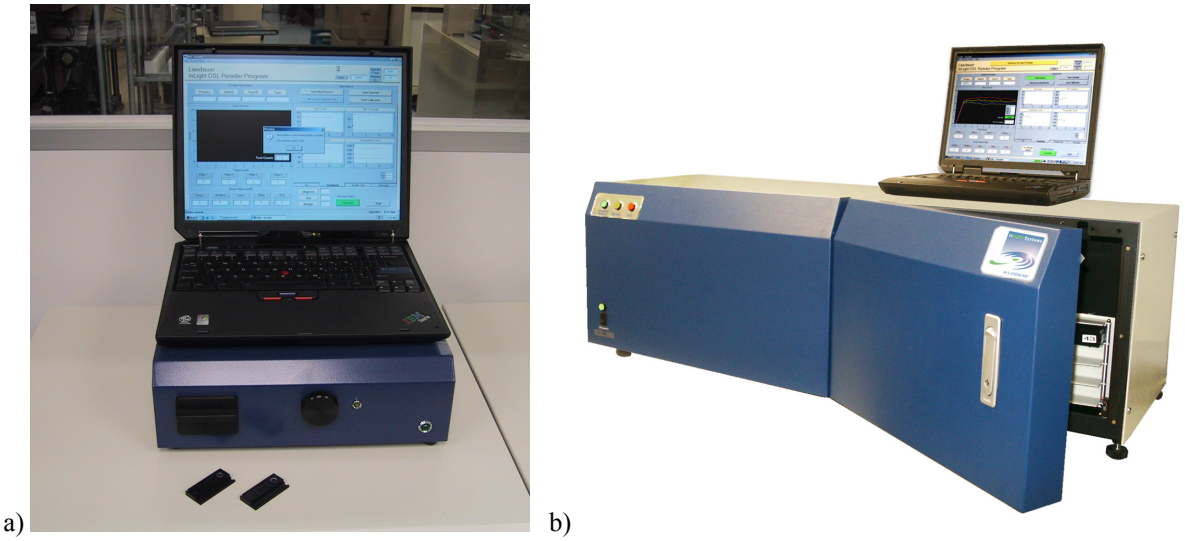

a) b)

FIGURE 26. Landauer OSL instrumentation: a) microStar manual OSL reader and b) InLight™ Auto200 reader with a 200 dosimeter loading capacity.

One of the first successful applications of OSL was in retrospective and accidental dosimetry [5,43] and today Model DA-20 TL/OSL reader developed and produced by RISOE National Laboratory, Denmark (Fig. 27) is considered the best tool for OSL research in dating and retrospective dosimetry [81,82]. The standard OSL stimulation head accommodates either one or several clusters of LEDs with different wavelengths of stimulation. A low dark count photomultiplier tube (PMT) is typically used as a photodetector. The combination of excitation cut-off and detection (usually band-pass) filters allow for good optical discrimination of stimulation and emission light. Multiple samples loaded on the carousel, a beta radioactive source or miniature X-ray tube, heating element and several OSL stimulation options allow for complex irradiation-reading-annealing profiles. Other modifications of the RISOE instrument are equipped with a laser and translation stages allowing for precise positioning and stimulation of single grains [5]. A compact OSL reader for extraterrestrial geological dating is also in the works [81].

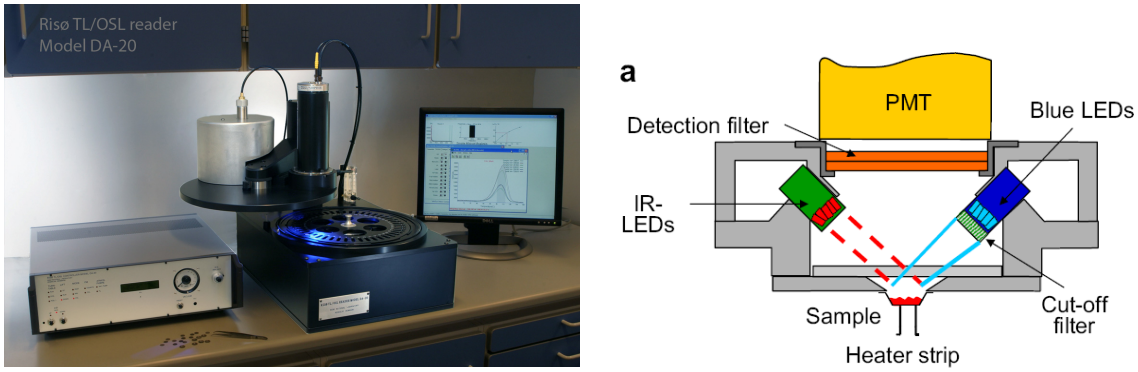

FIGURE 27. TL/OSL reader Model DA20 from RISOE National Laboratory, Denmark and diagram of the OSL head [81].

Yet another important application of OSL technology is remote fiber-optic dosimetry using miniature Al_2O_3:C sensors coupled to a fiber and to a portable OSL reader (Fig. 28). Al_2O_3 fiber sensors for remote, real-time dosimetry applications should exhibit several important characteristics. In addition to the usual requirements of high sensitivity and linearity of dose response they should demonstrate low concentrations of shallow and deep traps.

These last two requirements are especially important. The existence of shallow traps slows down the readout process during periodic stimulation, whereas charge accumulated on deep traps is difficult to bleach. One example of real-time dose rate measurements using RL and "equilibrium" OSL signals from Al_2O_3:C fiber sensors is presented in Fig. 29. More details about this new exciting technology can be found elsewhere in this book in the paper by Claus Andersen [26].

a) 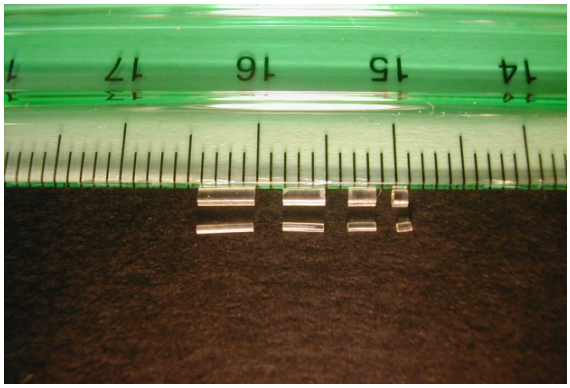 b) 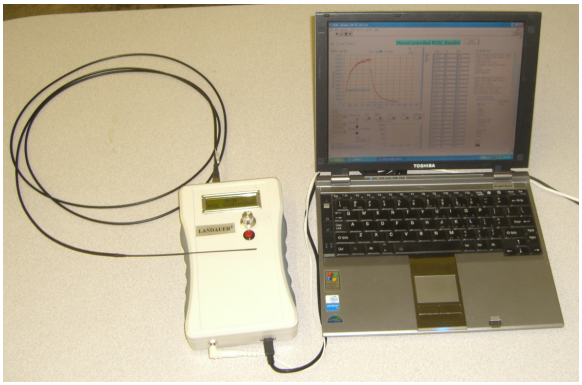

FIGURE 28. Al_2O_3:C fiber sensors (a), and portable fiber-optic OSL reader (b) developed at Landauer for medical application.

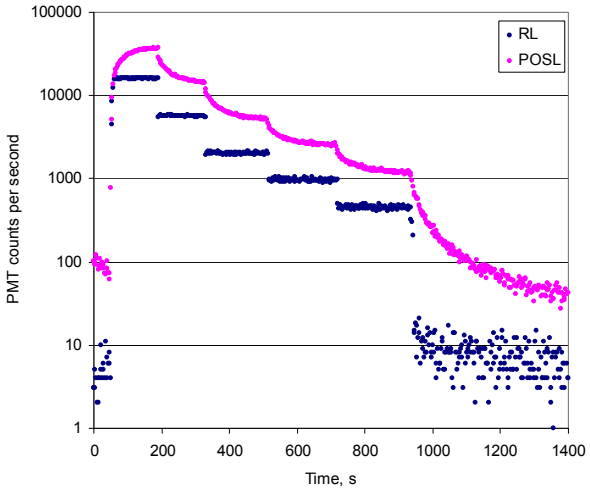

FIGURE 29. Real time dose rate measurements at 5 levels of X-ray tube current using fiber-optic instrument operating in combination of POSL and RL modes. Dose rate is proportional to both the intensity of RL signal, and to the equilibrium level of OSL.

4. BERYLLIUM OXIDE OSL DOSIMETRIC MATERIAL AND SYSTEMS

Until recently Al_2O_3:C and InLight™ OSL instrumentation from Landauer (USA) was the only widely used commercial OSL technology. Recent publications resulted from collaboration between Helmholtz-Zentrum (former GSF) in Munich and the Technical University of Dresden in Germany described the ongoing development of a personal dosimetry system based on BeO industrial ceramic detectors and a modular OSL reader system. The detector material - Thermalox 995™ (Brush Ceramic Products, Brush Wellman, Inc), that was used in this OSL system is a well known industrial ceramic previously investigated in 60s and 70s as a potential TL/TSEE detector [48-50]. BeO has been considered as an alternative dosimeter material which may compete with the LiF (TLD100) due to its near tissue-equivalence (Z_{eff}=7.14 vs Zeff ~ 7.6 for tissue) and high sensitivity, comparable to that of LiF.

At that time, it was rejected because of spurious excitations of background signal, light sensitivity and concerns over BeO toxicity.

The renewed interest in BeO was stimulated by the 1998 OSL study of BeO Termalox-995™ ceramic performed by Bulur and Göksu [51] where they demonstrated that the stimulation spectrum of the OSL signal is in a broad band ranging from 420 to 550 nm with a maximum near 435 nm. The emission spectra of the TL signal from BeO was reported to have a UV band with a main peak near 335 nm [3] and OSL emission was reported in a broad band around 325 nm [52]. The OSL reader developed by TU Dresden group (Fig. 30) uses 470 nm blue LEDs for stimulation and a Hamamatsu PMT for luminescence detections (Fig. 31). The emission from BeO shows thermal quenching at relatively low temperatures with an activation energy of 0.48- 0.52 eV [14] that might create some significant temperature dependence of OSL readout. Favorable dosimetric characteristics of BeO include a high sensitivity to ionizing radiation and a linear dose response over six orders of magnitude, from ~1 μGy to ~5 Gy (Fig. 32) and good photon energy response (Fig. 33) [52, 53].

The main concern for large volume application of BeO is that Termalox-995™ material is an industrial ceramic and the manufacturer does not have control of the impurities. As a result, the reproducibility of the chips properties is relatively poor. Calibration of every chip and assignment of the individual coefficient of sensitivity is probably required. BeO as well as Al_2O_3:C has some shallow and deep traps that produce phosphorescence just after irradiation and this might cause some problems in medical application in spite of BeO tissue equivalency. BeO toxicity is also a concern for in vivo medical applications.

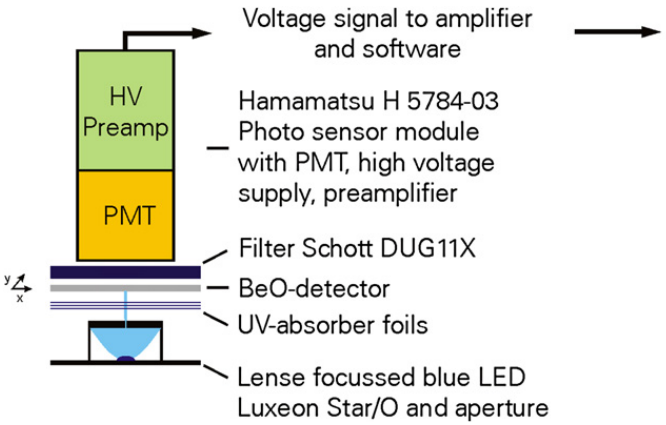

FIGURE 30. Schematic assembly of the BeO dosimetry system [83]

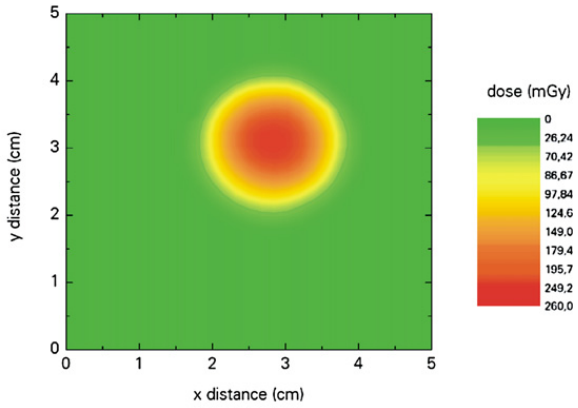

FIGURE 31. Example of measured dose distribution of collimated radiation source [83].

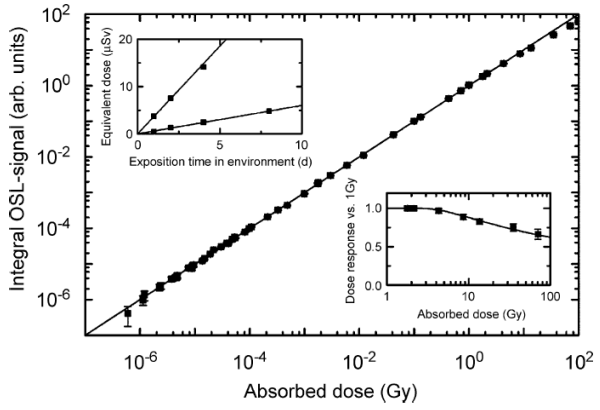

FIGURE 32. Dose dependence of BeO dosimeters with low detection limit of 1 μGy [53].

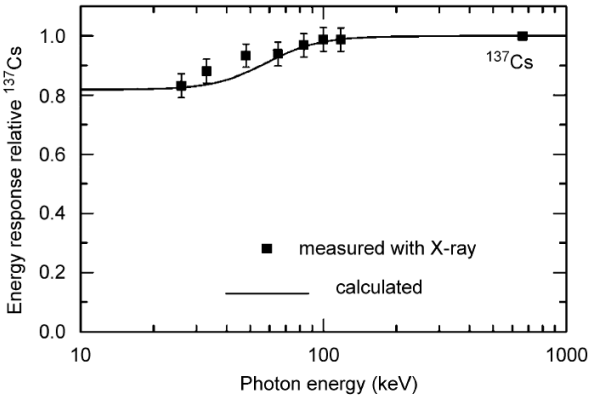

FIGURE 33. Energy response of BeO detectors is near tissue equivalent but still requires 20% correction at low photon energies [53].

5. FLUORESCENCE NUCLEAR TRACK DETECTORS

The radiation dosimetry community has long sought a dosimeter that overcomes the numerous limitations of current passive detector technology. Such a passive integrating detector would be sensitive to charged particles over a broad range of LET, require little or no post-exposure chemical processing, be capable of non-destructive (i.e. multiple) readouts using fully automated equipment, and possess the capability of being erased and reused. TL and OSL detectors, while fully reusable and highly sensitive to low-LET radiation, can only measure high-LET radiation of heavy charged particles (HCP) with reduced efficiency [78] and possess little or no sensitivity to fast neutrons [27,28]. In addition, TLD can only be read out a single time. CR-39 plastic nuclear track detectors (PNTD) [84,85] possess a sensitivity to radiation with LET in water ($LET_{\infty}H_2O$) above 5 keV/μm and to neutrons (via neutron-induced proton recoil tracks) [86], but lacks sensitivity to lower LET radiation. CR-39 PNTD can only be used once, and must be chemically etched prior to readout.

Novel Al_2O_3:C fluorescent nuclear track detectors, recently developed by Landauer, Inc., have demonstrated sensitivity and functionality superior to that of existing nuclear track detectors. The FNTD is based on single crystals of aluminum oxide doped with carbon and magnesium, and have aggregate oxygen vacancy defects (Al_2O_3:C,Mg) described in Section 3. Major advantages of Al_2O_3:C,Mg FNTD over conventionally processed CR-39 plastic nuclear track detector include superior spatial resolution, a wider range of LET sensitivity, no need for post-irradiation chemical processing of the detector, and the capability to anneal and reuse the detector. FNTDs show a low-LET threshold of 0.5 keV/μm, do not saturate at LET in water as high as 1800 keV/μm, and are capable of irradiation to fluences in excess of 10^6 cm^{-2} without saturation (track overlap). Expansion of the dose range and a solution for separation of neutron and gamma doses were demonstrated using three converter dosimeter designs and a new image processing technique in the spatial frequency domain.

5.1 Physics of Luminescence in Al_2O_3:C,Mg

The physics of FNTD is different from OSL and can be defined as a radio-photoluminescence (RPL), when radiation through radiochromic transformation of one type of color centers creates new stable luminescent centers that can be interrogated nondestructively with light through excitation-emission process without photo-ionization. In contrast with OSL where free electrons produce luminescence as a result of recombination on color centers (recombination luminescence), FNTD employs intracenter photoluminescence.

Al_2O_3:C,Mg crystals have green coloration due to a 435 nm absorption band caused by aggregate F_2^{2+}(2Mg) color centers consisting of two oxygen vacancies and charge-compensated by two magnesium ions (Fig 8) [38,39]. The electronic processes in Al_2O_3:C,Mg crystals are illustrated by Fig. 34. Ionizing radiation penetrating through the crystal creates a large number of electron-hole pairs. F_2^{2+}(2Mg) centers efficiently capture the free electrons and undergo radiochromic transformation into a three-electron state forming F_2^{+}(2Mg) centers. The center has an excitation band centered at 620 nm with 750 nm emission. Radiation-induced F_2^{+}(2Mg) color centers in the new material have an absorption band at 620 nm and produce fluorescence at 750 nm with a high quantum yield and a short, 75±5 ns, fluorescence lifetime suitable for fast scanning application.

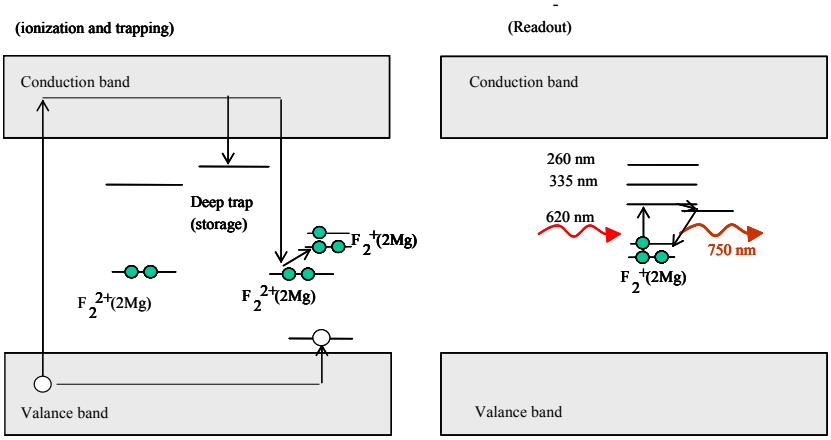

FIGURE 34. Flat band diagram of irradiation and readout of Al_2O_3:C,Mg [90].

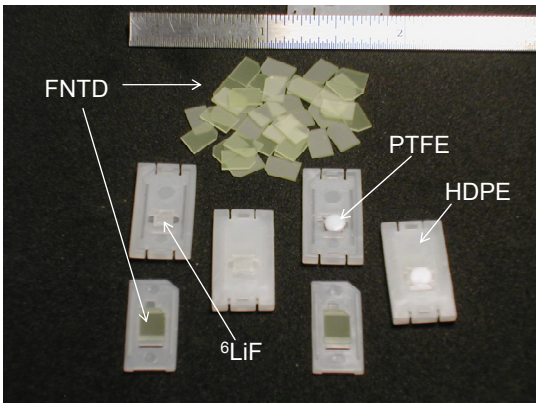

FIGURE 35. FNTDs and the PE converter cases with ^{6}LiF and PTFE chips. FNTDs were cut in the form of 6×4×0.5 mm^3 rectangular plates with the long side aligned along the optical *c*-axis of the crystal. One side of the FNTD was polished [33].

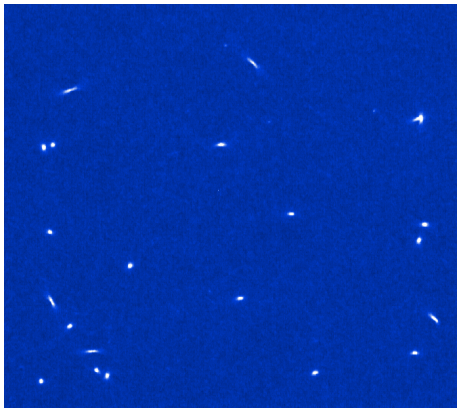

FIGURE 36. Example of fluorescent image with recoil proton tracks. FNTD was irradiated with ^{241}AmBe neutrons behind a polyethylene converter [36].

5.2 FNTD Dosimeter Configuration for Neutron-Gamma Separation

Track detectors, including FNTDs, have traditionally measured neutron dose by relating track density of nuclear reaction products to the incident neutron fluence. For thermal neutron detection, converters containing isotopes ^{6}Li or ^{10}B with a high capture cross-section are widely used [86]. For fast neutron detection, hydrogen, having the same mass as neutron, has the highest interaction cross-section [86]. For practical neutron dosimetry an FNTD crystal is covered by ^{6}LiF and/or polyethylene (PE) converters (Fig. 35). The reaction products - alpha particles, tritium ions or recoil protons produce ionization of Al_2O_3:C,Mg within the track volume and are imaged in fluorescent contrast as bright spots on dark background (Fig. 36) using a laser scanning readout system. At low doses and in the absence of high doses of photons, track recognition and track counting produces the best result and high sensitivity for neutron dose measurements [29, 32, 35].

Unlike PNTDs, Al_2O_3:C,Mg is also sensitive to low linear energy transfer (LET) radiation including secondary electrons resulting from interactions of photons with the crystal. Neutron radiation is usually accompanied by gamma radiation. If the dose of gamma radiation is above several cGy, then the fluorescence induced by overlapping secondary delta electron tracks can interfere with the signal induced by recoil protons making it difficult to detect and count neutron induced tracks [33]. A new image processing method will be described later in the paper as a technique to determine the correct dose in mixed gamma-neutrons fields.

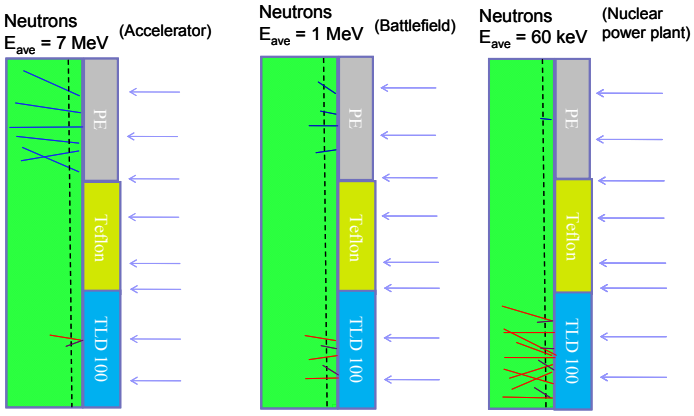

FIGURE 37. Diagram of FNTD-converter combinations illustrating energy response and neutron-gamma separation

It is common practice in neutron dosimetry to use two or three components in determining neutron dose in mixed fields. For example one component is sensitive to neutrons and gamma and the second component is sensitive only to gamma. Neutron dose is thus determined by:

$$D_n = \frac{Q(n+\gamma) - A(\gamma)D_\gamma}{B(n)}, \quad (5)$$

where $Q(n+\gamma)$ is the total response of the detector, $A(\gamma)$ is the sensitivity to gamma, D_γ is the gamma dose, and $B(n)$ is the sensitivity to neutrons [86].

For dosimetry of mixed fields FNTDs are mounted in polyethylene (PE) holders specifically designed to cover part of the polished side of the FNTD with PE and the other half with Polytetrafluoroethylene (PTFE or Teflon™) which does not contain hydrogen (Figs. 35 and 37). Images obtained behind PTFE provided signal from the photon dose whereas images behind PE provide information about both neutrons and photons. The purpose of the PTFE converter was to protect FNTD surface from recoil protons and provide electron equilibrium at the detector surface similar to PE during gamma irradiation. To further separate thermal/moderated and fast neutrons another converter made of LiF chips is used. At low energies of neutrons the track density behind LiF would be higher than behind PE converter, whereas for high energy neutrons it is an opposite trend that will be explained further in Neutron Energy Dependence section 5.6.2.

5.3 Readout System

Non-destructive readout of the detector is performed using a confocal laser scanning fluorescent microscopy technique. Scanning of the three-dimensional spatial distribution of fluorescent intensity along the track of a heavy charged particle (HCP) permits reconstruction of particle trajectories through the crystal and LET can be determined as a function of distance along the trajectory based on fluorescent intensity. FNTDs are imaged with a confocal laser scanning imaging system described in detail elsewhere [29,36].

Figs. 38 and 39 depict the optical diagrams of two in-house built confocal scanning systems designed to acquire fluorescence images from the detectors with near-diffraction limited resolution. The system in Fig. 39 uses the fiber-optically coupled diode laser with a wavelength λ = 635 nm and high numerical aperture (NA) 40X, 0.95NA objective lens. Two-axis galvanometer mirrors are used for a high scanning rate in the XY plane. Axial (Z) scanning and focal point depth positioning in the crystal is provided by a piezo-actuator stage. The fluorescence excited by the laser light is collected by the same objective lens, transmitted back through the dichroic mirror, imaged on a confocal pinhole and detected by a silicon avalanche photodiode (APD) installed behind the pinhole. An additional optical filter in front of the APD rejects residual laser light. The confocal pinhole is a spatial filter, blocking all fluorescence originating outside of the focal spot of the objective lens and providing diffraction limited spatial discrimination. Images are formed as an array of voltages obtained by the data acquisition board from the photodetector.

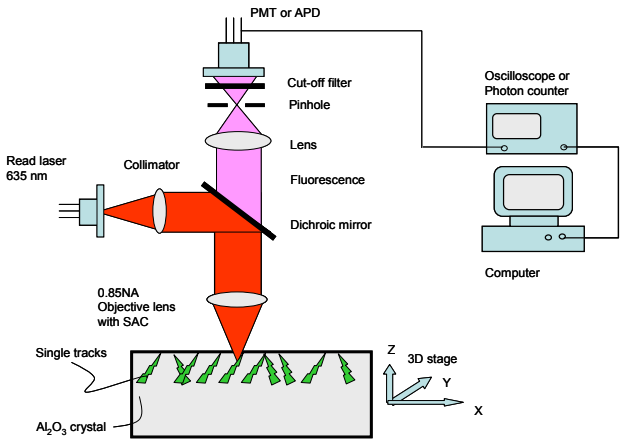

FIGURE 38. Diagram of the original confocal imaging system used for obtaining the first results (alpha particle images and preliminary LET dependences) with FNTDs [29].

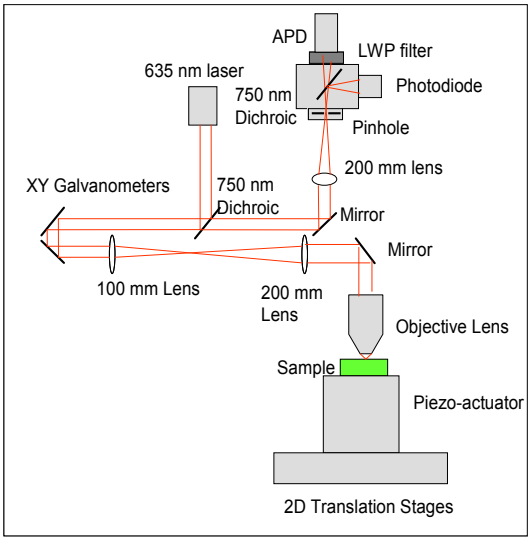

FIGURE 39. Optical diagram of the latest FNTD reader with fast scanning galvanometers and translation stages for multiple detector readout [36].

During readout, FNTDs are first scanned with the laser beam perpendicular to the detector surface to determine the surface position with an accuracy of 0.1 μm. After the axial surface position was found, the detectors are scanned in a plane parallel to their surface at a depth of 3.5 μm below the surface of the crystal. Single images have dimensions of 100×100 μm^2 and the number of acquired images depends on the measured dose and is adaptively varied between 25 and 100 for each of the converter areas.

5.4 Track Counting Mode of Dose Determination

Determining the dose of neutrons in counting mode is relatively simple. The readout system acquires a predetermined number of images, image processing recognizes and counts fluorescent tracks and rejects any artifacts related to crystal defects and surface contaminations. The neutron dose is proportional to the density of tracks per unit area, and the calibration coefficient in tracks/(mm^2mSv) is determined during calibration of the dosimetry system using standard neutron fields. It was shown that the track density is linear with dose (Fig. 43). It should be emphasized that the calibration coefficient strongly depends on neutron energy and it will be discussed in Section 5.6.2.

5.5 Spatial Frequency Analysis Mode

Spatial frequency analysis provides a new approach to determine the dose of radiation through evaluation of the modulation of the fluorescence intensity within an image acquired from an irradiated detector. The modulation of fluorescence intensity is caused by non-uniform energy deposition and ionization produced by charged particles (either recoil protons or secondary electrons) through the Coulomb interaction with the FNTD. Quantitative evaluation of fluorescence intensity modulation is done using spatial frequency analysis of the image (Fig. 40). The image is converted into the spatial frequency domain by the discrete Fourier transform (DFT) defined by

$$F(k,l) = \frac{1}{N^2}\sum_{m=0}^{N-1}\sum_{n=0}^{N-1} f(m,n)\, e^{-\frac{2\pi i}{N}(km+ln)} \qquad (6)$$

where $f(m,n)$ is the intensity of the original image in the spatial domain at points m and n; k and l are spatial frequencies, and $F(0,0)$ represents the DC offset of the image. The two-dimensional DFT is separable such that the image needs only to go through two sets of one-dimensional Fourier transforms instead of a double sum. The number of calculations needed to completely transform the image is N^2. Using the fast Fourier transform (FFT) allows for a reduction in the number of calculations to $N \log_2 N$ while leaving the final result the same.

The power spectral density of the image is calculated by squaring the magnitude of the Fourier transform, i.e. $|F(k,l)|^2$. Integrating the power spectral density over the predefined frequency range gives the parameter called Power Spectrum Integral (PSI) or power of the image given by

$$P = \int_{k_0}^{k}\int_{l_0}^{l} |F(k,l)|^2 \, dkdl \qquad (7)$$

where k_0 and l_0 are the initial spatial frequencies of interest.

The PSI was found to be proportional to dose for different types of radiation (Fig. 43) [33].

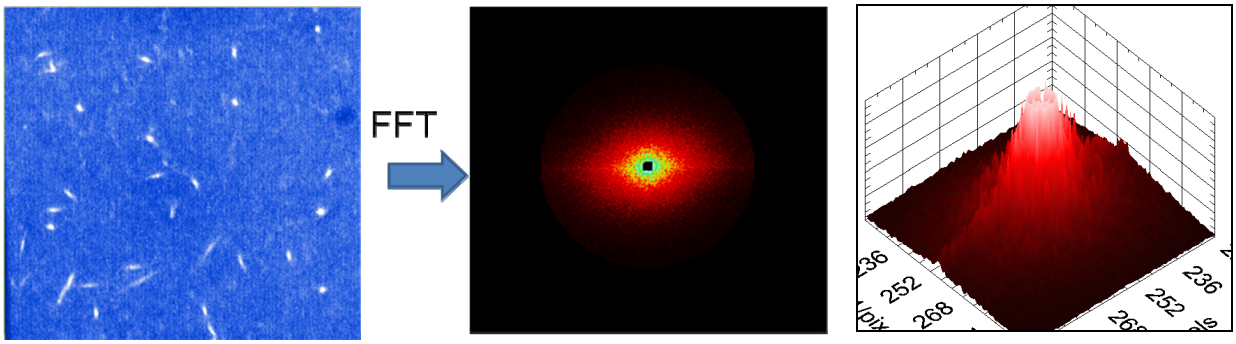

FIGURE 40. Fluorescent images are processed in spatial frequency domain and Power Spectrum Integral proportional to the absorbed dose is calculated [90].

Fluorescence images from the Al_2O_3:C,Mg crystal after medium and high doses of fast neutrons show a significant number of overlapping tracks (Fig. 41), that in the spatial frequency domain, should have a certain distinctive power spectrum. The same is true for medium and high doses of gamma radiation (Fig. 42). Although gamma photons may be incident on the crystal in a uniform manner, the amount and localization of energy deposition has a microscopic and statistical variation as described by a microdosimetric approach [87]. Tracks of individual secondary (or delta) electrons are in general invisible because of their low ionization density. With the increase of gamma dose they start overlapping and form bright features, which give the appearance of a "lumpy" texture on the image, and cause difficulty in identifying and counting recoil proton tracks.

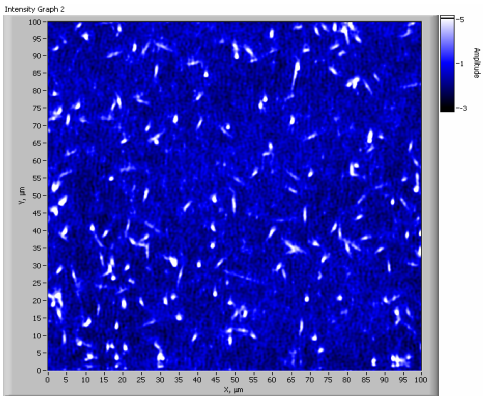

FIGURE 41. FNTD image after 1 Sv of fast neutrons from a bare ^{241}AmBe source (HDPE converter) [90].

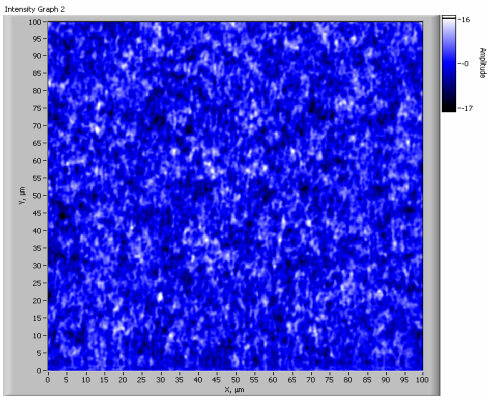

FIGURE 42. FNTD image after 2 Gy of 662 keV gamma from ^{137}Cs (Teflon™ converter) [90].

5.6 Dosimetric Properties of FNTD

5.6.1 Dose Dependences for Neutrons and Photons

Figure 43 illustrates the dose dependences of FNTDs irradiated with neutrons and gamma behind PE converter using two image processing modes: track counting mode and image power mode. It can be seen that the PSI is linear over a larger range of doses and allowed for an increase in saturation dose from 300 mSv using track counting to greater than 12 Sv using image power mode [36].

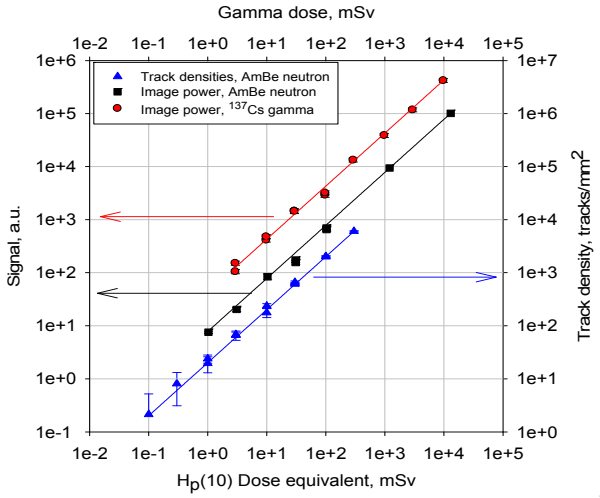

FIGURE 43. Dose dependences of FNTD behind PE converter for fast neutrons from a bare AmBe source using track counting (triangles) and image power mode (squares). Dose dependence of gamma induced signal using image power mode (circles) is also linear with dose [33].

The saturation dose for neutrons has not been reached because of low available AmBe source activity. The image power sensitivity of FNTDs (in terms of dose equivalent) to gamma (see *gamma response* below) is 5.6 times larger than the sensitivity to bare AmBe neutrons.

FNTDs irradiated with gamma and 40 kVp x-rays behind PE and PTFE converters demonstrated the linearity of dose response over a range of 5 orders of magnitude. The image power dependence for FNTDs irradiated with gamma behind PE and PTFE are nearly collinear. The difference in slopes between FNTDs covered with PE and PTFE is 2.5% which is attributed primarily to the difference in their mass absorption coefficients.

5.6.2 Energy dependence for monoenergetic and broad spectrum neutrons

Response of almost all neutron detectors strongly depends on neutron energy. The FNTD is not an exception. To obtain the calibration factors for monoenergetic and broad spectrum neutrons the irradiations were performed at the National Physics Laboratory (NPL) in the United Kingdom, at Pacific Northwest National Laboratories (PNNL), and at the Landauer irradiation facility in Illinois, USA. Two converters, PE and ^{6}LiF with different energy dependence of interaction cross sections were used and the calibration curves shown in Fig. 44 were obtained.

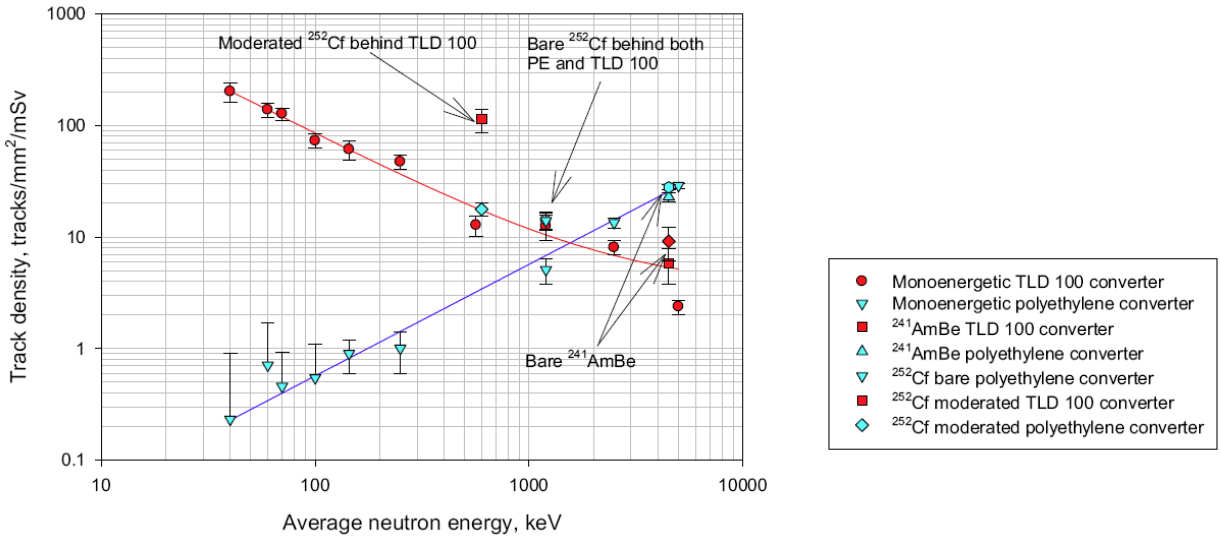

FIGURE 44. Track densities behind HDPE and LiF converters. Irradiations performed at NPL (UK) and PNNL (USA) [35].

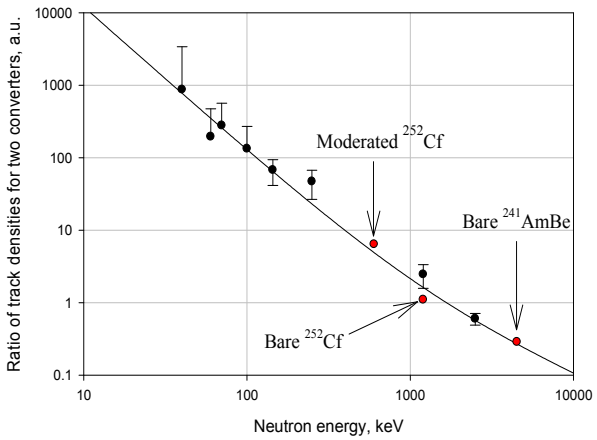

FIGURE 45. Ratio of track densities for monoenergetic and broad spectrum neutrons [35]

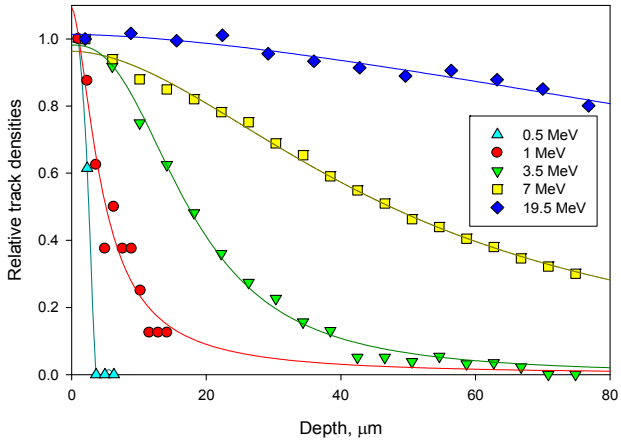

FIGURE 46. Track densities normalized to the track density at the surface for FNTDs covered with polyethylene as a function of scanning depth for high energy monoenergetic neutrons. Irradiations were performed at JRC-IRMM (Belgium) [35].

The energy dependence for LiF converters follow its (n,α) reaction cross-section well and track density decreases with increasing neutron energy, whereas the track density behind HDPE converters increases with increasing neutron energy. There are more recoil protons that make detectable tracks in the FNTD for higher energy neutrons due to increase of recoil proton range and their escape probability from a thick polyethylene converter. Track densities corresponding to the broad spectrum neutron sources (bare ^{241}AmBe, bare and moderated ^{252}Cf) are not necessarily expected to follow the same energy dependence as for mono-energetic neutrons because of the large amount of both low and high energy neutrons in their spectra. The ratio of track densities behind LiF and PE converters, plotted as a function of neutron energy (Fig. 45), is a smooth function of energy, and does not depend on the delivered dose. Therefore, it should serve as a good parameter to determine the median energy of incident neutrons for both monoenergetic and broad spectrum neutron sources.

Another interesting approach of neutron energy estimation using FNTD technology was demonstrated by using 3D capability of confocal detection. The detectors covered with PE converters were irradiated at the Joint Research Centre - Institute for Reference Materials and Measurements (JRC-IRMM) in Belgium with mono-energetic neutrons in the range of 500 keV to 19.5 MeV and then were imaged at different depths to obtain a depth profile of track density or power spectrum integral (Fig. 46). The depth profile of recoil proton induced signal is strongly dependent on the neutron energy and can be used for neutron energy estimation. The details of this study can be found in [35].

5.6.3 LET Dependence

It has been shown that FNTD can be used as a spectroscopic tool for identification of heavy charged particles. The dependence of fluorescence track amplitudes on LET and Z/β is smooth and easy to calibrate [37]. Figure 47 shows fluorescence amplitude distribution histograms for seven ions having different atomic number Z, energies and LET. The histograms clearly demonstrate the ability of FNTD to distinguish tracks caused by incident particles with differing $LET_{\infty H2O}$ values. The full-width at half maximum (FWHM) of the peaks can be thought of as the spectral resolution of the technology. The fluorescence amplitude has not yet reached saturation even at large LET values. Earlier experiments proved that FNTD are capable of detecting 250 MeV protons with $LET_{\infty H2O}$ of 0.4 keV/µm [29]. The dependence of fluorescence amplitude for all the heavy ion beams used in this study, both bare and behind wedge absorbers, is illustrated in Fig. 48. The dependence on LET is nonlinear and the continuing increase in fluorescence amplitude indicates that the detector has not saturated even at $LET_{\infty H2O}$ = 8767 keV/µm. Bragg peaks were obtained for a total of eight different types of ions using metal wedged absorbers [37]. The spectroscopic capabilities of FNTD technology can be of particular importance to radiobiology, radiotherapy, space and neutron dosimetry and nuclear reaction diagnostic experiments.

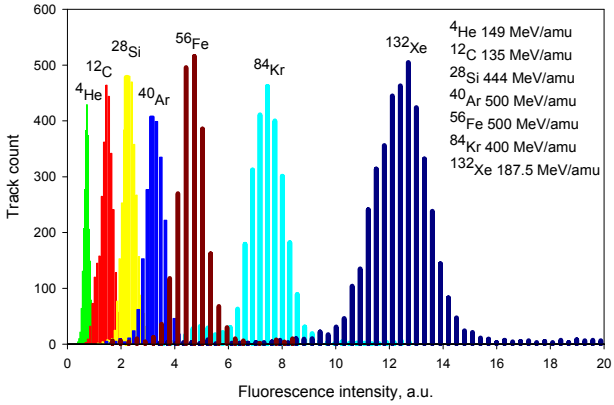

FIGURE 47. Fluorescence intensity distributions for seven high energy ions incident on bare FNTDs. The irradiations were performed at HIMAC, NIRS, Japan [37].

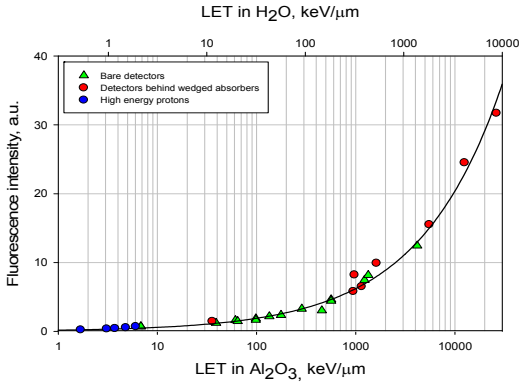

FIGURE 48. Fluorescence intensity dependence on LET_{∞} in aluminum oxide (bottom axis) and water (top axis). High energy protons are included for completeness [37].

5.7 Application of fluorescent Al_2O_3:C,Mg crystals for high resolution imaging in Microbeam Radiation Therapy (MRT)

Microbeam Radiation Therapy (MRT) is an experimental radiotherapy technique that has impressive preliminary results. MRT has the potential to treat infantile brain tumors when other kinds of radiotherapy would be excessively toxic to the developing normal brain. MRT uses extraordinarily high doses of X-rays but provides unusual resistance to radioneurotoxicity. By using highly collimated, quasi-parallel arrays of X-ray microbeams, produced by 3rd generation synchrotron sources, small beam divergence and steep dose gradient with a penumbra sharper than that achieved by conventional radiotherapy can be produced [88]. FNTDs look very promising for this new application (Fig. 49).

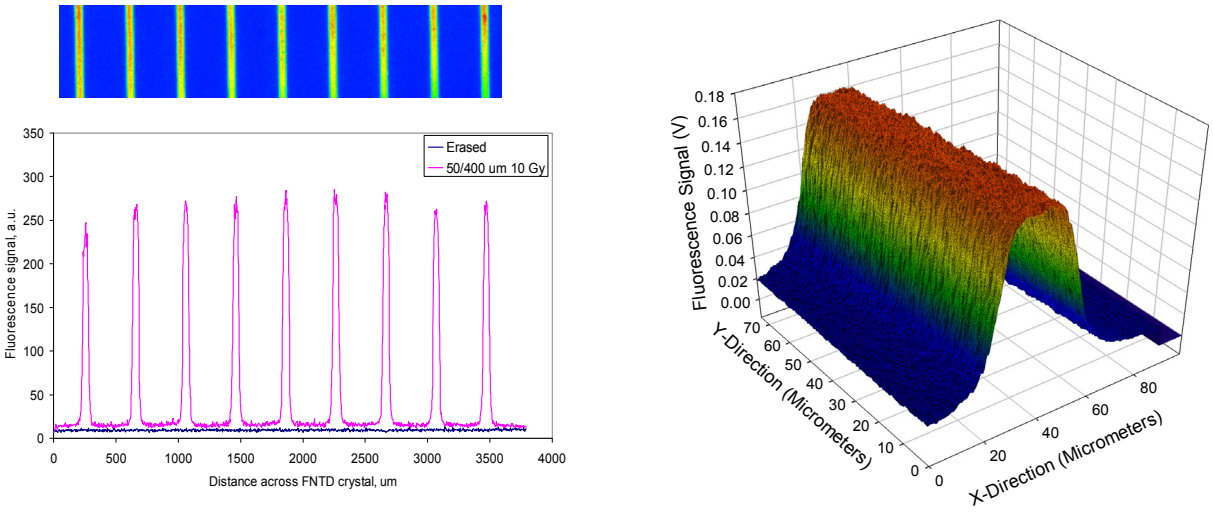

FIGURE 49. Fluorescent image and its cross-section after irradiating the Al_2O_3:C,Mg crystal with synchrotron microbeam and read using laser scanning confocal fluorescent imager. Detector was irradiated with 10 Gy of peak dose, with center-to center spacing of 400μm apart and 50μm FWHM [89].

FNTDs were optimized for imaging application in 4 orders of magnitude of photon doses ranging from 5 mGy to 50 Gy and spatial resolution of 0.6 micron. High spatial resolution and wide dynamic range of dose measurements make FNTD technology very attractive for MRT quality assurance application, when large peak-to-valley dose ratio (PVDR) has to be measured very precisely.

The European Synchrotron Radiation Facility (ESRF) produced highly collimated X-rays in the range 50-350 keV with median energy 107 keV. A number of FNTDs were irradiated with various doses and slit spacing. PVDRs were measured for 50 μm FWHM beams with center-to-center spacing from 50 to 400 μm at different doses from 3 to 100 Gy and at 1, 11, 21 and 31 mm depth in a PMMA phantom. A wide dynamic range of measured doses and high resolution 2D imaging of microbeam fields were demonstrated [89].

6. SUMMARY AND CONCLUSIONS

The OSL technique already became a successful tool in personal radiation dosimetry, geological and archeological dating, and in radiation diagnostic imaging. Significant advances were made recently in theoretical study of OSL that explains the behavior of radiation sensitive materials with several types of dosimetry traps, recombination centers and competing shallow deep traps. Progress in material, detector and instrumentation engineering allowed for new promising developments of OSL applications in the medical field.

We described in detail the physics and dosimetric performance of Al_2O_3:C. High sensitivity, wide dynamic range of dose measurements, extremely low limit of detection (LLD) of 0.4 μGy, negligible thermal fading, and good environmental stability of Al_2O_3:C make it the most popular OSL detector for different applications including occupational monitoring and different aspects of medical dosimetry.

The next technological breakthrough was done with Fluorescent Nuclear Track Detectors that have some important advantages in measuring fast neutron and high energy heavy charge particles that became the latest tool in

radiation therapy. New Mg-doped aluminum oxide crystals and novel type of imaging instrumentation for FNTD technology were discussed with regard to application in mixed neutron-gamma fields, medical dosimetry and radiobiological research. FNTD is a passive integrating type of detector that does not require wires, electronics or batteries during irradiation. This detector is immune to electromagnetic interference and can measure doses at very high dose rate (was successfully tested at 10^8 Gy/s). FNTD detectors are made of sapphire and provide extremely good temperature and environmental stability, no light sensitivity, thermal fading or signal build-up. FNTD imaging plates are reusable after thermal annealing or optical bleaching. The FNTD readout process is completely optical and non-destructive with no chemical etching or other detector preparation. Fast automatic scanning, image processing and track counting software was developed and implemented. Separation of fast and moderated neutron doses as well as neutrons and photons was achieved through the use of three different converters and novel image processing technique.

FNTD technology allows for fast and inexpensive assessment of average neutron energies in facilities by using depth profile or the ratio of track densities behind two converters. Neutron detection efficiency of FNTDs is comparable with CR-39. At the same time FNTDs are sensitive to high energy neutrons (20-100 MeV) where CR-39 detectors loose its response because of low sensitivity to high energy recoil protons with LET less than 5 keV/μm. Saturation dose for FNTDs is more than 1000 times higher than for CR-39 PNTDs. Compact table-top FNTD instrument for automatic detector processing is under development.

ACKNOWLEDGMENTS

The author would like to thank all his colleagues at Landauer and Oklahoma State University, including professors and students, who contributed enormously to development of all aspects of OSL and FNTD technologies from crystal growth and spectroscopic studies, to design of readout instruments and dosimeters. I also want to acknowledge the contributions and insightful discussions of my collaborators from other institution: RISOE (Denmark), NIRS (Japan), ESRF (France), RARAF-Columbia University and many others.

REFERENCES

1. S.W.S. McKeever, *Thermoluminescence of solids*, Cambridge: Cambridge University Press, 1985.
2. Bräunlich, P. *Introduction and basic principles*. In: *Thermally stimulated relaxation in solids*. (Ed.: Bräunlich, P.) Berlin Springer Verlag, 1979.
3. S.W.S. McKeever, , M. Moscovitch, and P.D. Townsend, *Thermoluminescence dosimetry materials: Properties and uses.* Ashford: Nucl. Tech. Pub., 1995.
4. R. Chen, S.W.S. McKeever, *Theory of thermoluminscence and related phenomena*, Singapore: World Scientific Pub., 1997.
5. L. Bøtter-Jensen, A.G. Wintle, and S.W.S. McKeever, *Optically stimulated luminescence dosimetry*. Amsterdam: Elsevier, 2003.
6. J. Gasiot, P. Bräunlich1, and J.P. Fillard, *Laser heating in thermoluminescence dosimetry,* J. Appl. Phys. **53**, 5200-5209 (1982).
7. M.S. Akselrod, V.S. Kortov, D.J. Kravetsky, V. I. Gotlib, *Highly sensitive thermoluminescent anion-defective α-Al_2O_3:C single crystal detectors*, Radiat. Prot. Dosim. **32**, 15-20 (1990).
8. M.S. Akselrod and E.A. Gorelova, *Deep traps in highly sensitive α-Al_2O_3:C TL crystals,* Nucl. Tracks Radiat. Meas. **21**, 143-146 (1993).
9. M.S. Akselrod and V.S. Kortov, *Thermoluminescent and exoemission properties of new high sensitivity TLD α-Al_2O_3:C Crystals*, Radiat. Prot. Dosim. **33**(1-4), 123-126 (1990).
10. S.W.S. McKeever, M.S. Akselrod and B.G. Markey, *Pulsed optically stimulated luminescence dosimetry using α-Al_2O_3:C*, Radiat. Prot. Dosim. **65**, 267-272 (1996).
11. M.S. Akselrod, A.C. Lucas, J.C. Pulf, and S.W.S. McKeever, *Optically stimulated luminescence of Al_2O_3*, Radiat. Meas. **29**, 391-398. (1998).
12. M.S. Akselrod, and S.W.S. McKeever, *A radiation dosimetry method using pulsed optically stimulated luminescence*, Radiat. Prot. Dosim. **81**, 167-176 (1999).
13. M.S. Akselrod, N. Agersnap-Larsen, V. Whitley and S.W.S. McKeever, *Thermal quenching of F-centre luminescence in Al_2O_3:C,* J. Appl. Phys. **84**, 3364-3373 (1998).
14. E. Bulur and A. Yeltik, *Optically stimulated luminescence from BeO ceramics: An LM-OSL study,* Radiat. Meas. **45**, 29–34 (2010).
15. M. Sonada, M. Takano, J. Miyahara, and H. Kato, *Computed radiography utilizing scanning laser stimulated luminescence*. Radiography **148,** 833-837 (1983).

16. M.S. Akselrod, N. Agersnap Larsen, and S.W.S. McKeever, *A procedure for the distinction between static and dynamic radiation exposures of personal radiation badges using pulsed optically stimulated luminescence,* Radiat. Meas., **32**, 215-225 (2000).
17. R.E. Creager and P.K. Soltani, *Fiber optic dosimeter using electron trapping materials employing technique for eliminating background fluorescence,* US Patent #5,091,653 (1992).
18. J.C. Polf, , S.W.S. McKeever, M.S. Akselrod, and S. Holmstrom, *A real-time, fiber optic dosimetry system using Al_2O_3 fibers*. Radiat. Prot. Dosim. **100**, 301-304 (2002).
19. J.C. Polf, , E.G. Yukihara, , M.S. Akselrod, , and S.W.S. McKeever, *Real-time luminescence from Al_2O_3 fiber dosimeters,* Radiat. Meas. **38**, 227-240 (2004).
20. M.C. Aznar, C.E. Andersen, L. Bøtter-Jensen, S.A.J. Bäck, S. Mattsson, F. Kjær-Kristoffersen, and J. Medin, *Real-time optical fiber luminescence dosimetry for radiotherapy: physical characteristics and applications in photon beams,* Phys. Med. Biol. **49**, 1655–1669 (2004).
21. M.C. Aznar, , J.C. Polf, M.S. Akselrod, C.E. Andersen, , S.A.J. Back, , L. Bøtter-Jensen, , S. Mattson, S.W.S. McKeever, and J. Medin, *Real-time optical fiber dosimetry in radiotherapy*. Presented at 44th AAPM, Montreal, Canada, In: Med. Phys. **29**, 1371 (2002).
22. M.S. Akselrod, S.W.S. McKeever, and L. Botter-Jensen, *Optically stimulated luminescence and its use in medical dosimetry*, Radiat. Meas. **41,** S78-S99 (2007).
23. B.L. Justus, K.J. Pawlovich, C.D. Merritt, and A.L. Huston, *Optically and thermally stimulated luminescence characteristics of Cu^+-doped fused quartz.* Radiat. Prot. Dosim. **81**, 5-10 (1999).
24. A.L. Huston, B.L. Justus, P.L. Falkenstein, R.W. Miller, H. Ing, and R. Altemus *Remote optical fibre dosimetry.* Nucl. Instr. Meth. B**, 184**, 55-77 (2001).
25. G. Ranchoux, S. Magne, J.P. Bouvet, and P. Ferdinand, *Fiber remote optoelectronic gamma dosimetry based on optically stimulated luminescence of Al_2O_3:C.* Radiat. Prot. Dosim. **100,** 255-260 (2002).
26. C. Anderson, *RL and OSL Dosimetry and its medical application,* AIP, These Proceedings, 2010.
27. J.C.R. Mittani, A.A.R.d Silva, F. Vanhavere, M.S.,, Akselrod, E.G. Yukihara, *Investigation of neutron converters for production of optically stimulated luminescence (OSL) neutron dosimeters using Al_2O_3:C.* Nucl. Instr. Meth. B, **260,** 663-671 (2007).
28. E.G. Yukihara, J.C. Mittani, F. Vanhavere, and M.S Akselrod, *Development of new optically stimulated neutron dosimeters*. Radiat. Meas. **43,** 309-314 (2008).
29. G. M. Akselrod, M. S. Akselrod, E. R. Benton, and N. Yasuda, *A Novel Al_2O_3 fluorescent nuclear track detector for heavy charged particles and neutrons,* Nucl. Instr. Meth. B **247,** 296-306 (2006).
30. M. S. Akselrod, A. E. Akselrod, *New Al_2O_3:C,Mg crystals for radiophotoluminescent dosimetry and optical imaging of tracks produced by heavy charge particles*, Radiat Prot. Dosim. **119** (1-4), 218-221 (2006).
31. M. S Akselrod, R. C. Yoder, G. M. Akselrod, *Confocal fluorescent imaging of tracks from heavy charged particles utilizing new Al_2O_3:C,Mg crystals*, Rad. Prot. Dosim. **119**(1-4), 357-362 (2006).
32. G.J. Sykora, M.S. Akselrod, M. Salasky, S.A. Marino *Novel Al2O3:C,Mg fluorescence nuclear track detectors for passive neutron dosimetry.* Radiat. Prot. Dosim. **126**, 278-283 (2007).
33. G.J. Sykora and M.S. Akselrod, *Novel fluorescent nuclear track detector technology for mixed neutron-gamma fields*, Radiation Measurements., Radiat. Meas. **45** (3-6), 594-598 (2010).
34. G.J. Sykora and M.S. Akselrod, , *Photoluminescence study of photochromically and radiochromically transformed Al_2O_3:C,Mg crystals used for fluorescent nuclear track detectors,* Radiat. Meas. **45** (3-6), 631-634 (2010).
35. G.J., Sykora, M.S. Akselrod, F.Vanhavere, *Performance of fluorescence nuclear track detectors in monoenergetic and broad spectrum neutron fields*. Radiat. Meas. **44**, 988-991 (2009).
36. G.J. Sykora, M. Salasky, , and M.S. Akselrod, *Properties of novel fluorescent nuclear track detectors for use in passive neutron dosimetry*, Radiat. Meas. **43**, 1017-1023 (2008).
37. G.J. Sykora, M.S. Akselrod, E.R. Benton, and N. Yasuda, *Spectroscopic properties of novel fluorescent nuclear track detectors for high and low LET charged particles*, Radiat. Meas. **43**, 422-426 (2008).
38. M. S. Akselrod, A. E. Akselrod, S.S. Orlov, S. Sanyal and T.H. Underwood, *Fluorescent aluminum oxide crystals for volumetric optical Data Storage and Imaging Applications,* J. of Fluorescence, **13,** 503-511 (2003).
39. S. Sanyal and M. S. Akselrod, *Anisotropy of optical absorption and fluorescence in Al_2O_3:C,Mg crystals*, J. Appl. Phys. **98**, 033518 (2005).
40. A. Diaspro, Ed., *Confocal and two-photon microscopy: Foundations, applications, and advances,* New-York: Wiley, 2002.
41. V.V. Antonov-Romanovskii, I.B. Keirum-Marcus, M.S. Poroshina, and Z.A. Trapeznikova, *IR stimulable phosphors*, In: *Conference of the Academy of Sciences of the USSR on the Peaceful Uses of Atomic Energy,* Moscow, 1955. USAEC Report AEC-tr-2435, 239-250 (1956).
42. E.N. Sanborn and E.L. Beard, *Sulfides of strontium, calcium, and magnesium in infrared-stimulated luminescence dosimetry.* In: Proc. 1st Int. Conf. on Luminescence Dosimetry, Stanford, June 1965, USAEC, 183-191, (1967).
43. D.J. Huntley, D.L. Godfrey-Smith, and M.L.W. Thewalt, *Optical dating of sediments.* Nature **313,** 105-107 (1985).
44. A. Meijerink, W.J. Schipper, and G. Blasse, *Photostimulated luminescence and thermally stimulated luminescence of Y_2SiO_5-Ce, Sm.* J. Phys. D **24**, 997-1002 (1991).
45. W.J. Schipper, J.J. Hamelink, and G. Blasse, *The X-Ray storage properties of barium phosphate doped with trivalent rare earth ions.* Phys. Stat. Sol. (a) **141,** 231-238 (1994).

46. L.E. Trinkler, M.F. Trinkler, and A.I. Popov, *Stimulation Energy of the X-Ray Storage Material KBr: In.* Phys. Stat. Sol. (b) **180,** K31-K34 (1993).
47. H.O. Albrecht, C.E. Mandeville, *Storage of energy in BeO*. Phys. Rev. 101, 1250 (1956).
48. E. Tochilin, N. Goldstein, and W.G. Miller, *Beryllium oxide as a thermoluminescent dosimeter,* Health Phys. **16**, 1-7 (1969).
49. G. Scarpa, The dosimetric use of beryllium oxide as a thermoluminescent material: A preliminary study. Phys. Med. Biol. **15,** 667-672 (1970).
50. R. B. Gammage, K.W. Crase, K. Becker, *Role of Silicon Activator in Exoelectron Emission from BeO*, Health Phys. **22**(1), 57-63 (1972).
51. E. Bulur, , H.Y. Göksu, *OSL from BeO ceramics: new observations from an old material.* Radiat. Meas. **29**, 639-650 (1998).
52. M. Sommer and J. Henniger, *Investigations of a BeO-based optically stimulation luminescence dosimeter.* Radiat. Prot. Dosim. **119**, 394–397 (2006).
53. M. Sommer, , R. Freudenberg, , J. Henniger, *New aspects of a BeO-based optically stimulated luminescence dosimeter*. Radiat. Meas. **42**, 617–620 (2007).
54. M. Sommer, A. Jahn, J. Henniger, *Beryllium oxide as optically stimulated luminescence dosimeter*, Radiat. Meas. **43**, 353–356 (2008).
55. A.S. Pradhan and K. Ayyangar, *Radiation dosimetry by photostimulated luminescence of $CaSO_4$: Dy.* Int. J. Appl. Radiat. Isotopes **28,** 534-535 (1977).
56. R. Bernhardt and L. Herforth, *Radiation dosimetry by optically stimulated phosphorescence of CaF_2:Mn.* In*:* Proc. 4th Int. Conf. Lumin. Dosimetry. Krakow, Poland, 1091-1104 (1974).
57. S.D. Miller, G.W.R. Endres, J.C. McDonald, and K.L. Swinth, *Cooled optically stimulated luminescence in CaF_2:Mn.* Radiat. Prot. Dosim.*,* **25,** 201-205 (1988).
58. R.C. Yoder, and M.R. Salasky, *A dosimetry system based on delayed optically stimulated luminescence.* Health Phys*.* **72,** S18-S19 (1997).
59. E. Bulur, *An alternative technique for the optically stimulated luminescence experiment*. Radiat. Meas. **26**, 701–709 (1996).
60. A.M. Stoneham, *Theory of defects in solids.* Oxford: Clarendon Press, 1975.
61. P. Braunlich, D. Schafer, and A. Scharmann, *A simple model for thermoluminescence and thermally stimulated conductivity of inorganic photoconducting phosphors and experiments pertaining to infra-red stimulated luminescence*. In: Proc. 1st Int. Conf. on Luminescence Dosimetry, Stanford, June 1965, USAEC, 57-73 (1967).
62. J.K. Rieke, and F. Daniels, *Thermoluminescence studies of aluminum oxide*. J. Phys**.** Chem.**, 61**, 629-633 (1957).
63. W.G. Buckman, *Aluminum oxide thermoluminescence properties for detecting radiation*, Health Phys. **22**,.402-402 (1972).
64. R.S. McDougall, and S. Rudin, *Thermoluminescent dosimetry of aluminum oxide.* Health Physics, **19**, 281-283 (1970).
65. S.K. Mehta, and S. Sengupta, *Gamma dosimetry using Al_2O_3:Si,Ti thermoluminescent phosphor*. Phys. Med. Biol., **21**, 955-964 (1976).
66. M. Osvay, and T. Biro, *Aluminum oxide in TL dosimetry.* Nucl. Instr. Meth., **175**, 60-61 (1980).
67. D. Lapraz, P., Iacconi, Y. Sayady, P. Keller, J. Barthe, and G. Portal, *Some thermoluminescence of an α-Al_2O_3 sample,* Phys. Stat. Sol. (a) **108**, 783-794 (1988).
68. P. Pokorny and A. Ibarra, *On the origin of the thermoluminescence of α-Al_2O_3: Cr, Ni.* J. Phys.: Condens. Matter, **5**, 7387-7396 (1993).
69. B. D. Evans and M. Stapelbroek, *Optical properties of the F^+ centre in crystalline Al_2O_3.* Phys. Rev. B **18**, 7089-7098 (1978).
70. K. H. Lee and J. H. Crawford, *Electron centers in single crystal Al_2O_3*, Phys. Rev. B **15**, 4065-4074 (1977).
71. L. E.Colyott, M.S. Akselrod, and S.W.S. McKeever, *Phototransferred thermoluminescence in α-Al_2O_3,* Radiat. Prot. Dosim*.* **65** 263-266 (1996).
72. E. G. Yukihara, V.H. Whitley, S.W.S. McKeever, A.E. Akselrod, and M.S. Akselrod, *Effect of high-dose irradiation on the optically stimulated luminescence of Al_2O_3:C.* Rad. Meas. **38**, 317-330 (2004).
73. S.W.S. McKeever, *Optically Stimulated Luminescence Dosimetry.* Nucl. Instrum. Meth. B. **184**, 29-54 (2001).
74. S.W.S. McKeever and M. Moscovitch, *On the advantages and disadvantages of optically stimulated luminescence dosimetry and thermoluminescence dosimetry*. Radiat. Prot. Dosim. **104**, 263-270 (2003).
75. V.H. Whitley and S.W.S. McKeever, *Photoionization of deep centers in Al_2O_3*. J. Appl. Phys. **87**, 249-256 (2000).
76. E.G. Yukihara, V.H. Whitley, J.C. Polf, D.M. Klein, S.W.S. McKeever, A. E., Akselrod, M. S. Akselrod, *The effects of deep trap population on the thermoluminescence of Al_2O_3:C*, Radiat. Meas. **37**, 627-638 (2003).
77. G. Molnar, M. Benabdesselam, J. Borossay, P. Iacconi, D. Lapraz, and M.S. Akselrod*, Influence of the irradiation temperature on the dosimetric and high temperature TL peaks of Al_2O_3:C*, Radiat. Prot. Dosim. **100**, 139-142 (2002).
78. E. G. Yukihara, R. Gaza, S.W.S. McKeever, and C.G. Soares, *Optically stimulated luminescence and thermoluminescence efficiencies for high-energy heavy charged particle irradiation in Al_2O_3:C.* Rad. Meas. **38**, 59-70 (2004).
79. C. Passmore, M. Kirr, and M. Salasky. Internal Landauer report, (2008).
80. E.G. Yukihara et al. OSU-Landauer internal report, (2008).
81. L. Bøtter-Jensen, K.J.Thomsen,M.Jain *Review of optically stimulated luminescence (OSL)instrumental developments for retrospective dosimetry* Radiat. Meas. **45** 253–257 (2010).
82. K.J. Thomsen, L. Bøtter-Jensen, M. Jain, P.M. Denby, A.S. Murray, *Recent instrumental developments for trapped electron dosimetry.* Radiat. Meas. **43**, 414–421 (2008).
83. A. Jahn, M. Sommer, J. Henniger, *2D-OSL-dosimetry with beryllium oxide*, Radiat. Meas. **45,** 674-676 (2010).

84. E. R. Benton, E. V. Benton, A. L. Frank, *Passive dosimetry aboard the Mir Orbital Station: internal measurements,* Radiat. Meas. **35**(5) 443-460 (2002).
85. E. V. Benton, R.A. Oswald, A. L. Frank, R.V. Wheeler, *Proton-recoil neutron dosimeter for personnel monitoring*, Health Phys. **40** 801-809 (1981).
86. F.H. Attix. Introduction to radiological physics and radiation dosimetry, New York: John Wiley & Sons, 1986 pp. 476-477.
87. H.H. Rossi and M. Zaider, Microdosiemtry and its applications, Berlin: Springer, 1996.
88. D.N. Slatkin, et al., Proc. Natl. Acad. Sci. USA 92, 8783-8787 (1995).
89. J. Bartz, G.J. Sykora and E. Brauer-Krisch, M.S. Akselrod, *Imaging and dosimetry of synchrotron microbeams with aluminum oxide fluorescent detectors,* Book of Abstracts, SSD-16 conference, Sydney (2010).
90. G.J. Sykora, *Photo- and radiochromic transformations in Al_2O_3:C, Mg fluorescent nuclear track detectors and high resolution imaging of radiation fields,* Ph.D. Dissertation, Oklahoma State University, Feb., 2010.